

1 The figure captions can still be improved, e.g.
2 Fig.2: the sub-domain in 1 is the study area. Then you don't need to repeat in other figures
3 caption.
4 **We deleted the sentence in the figure captions except for Figure 2.**
5 In many figures caption, you stated the same text: "without removing,", you can write it in the
6 text
7 We deleted the expression, and added a sentence at the end of the first paragraph in the section
8 Datasets and methods ("In our analyses, we remain the trends in the data over the 1979-2019
9 period.").
10 Fig.7: red line is the trend.
11 **We changed it.**

12
13
14
15
16
17
18
19
20
21
22
23
24
25
26
27
28

29 Revisiting the trend in the occurrences of the “warm Arctic-cold Eurasian continent”

30 **temperature pattern**

31 Lejiang Yu^{1,2*}, Shiyuan Zhong³, Cuijuan Sui⁴, and Bo Sun¹

32 1MNR Key Laboratory for Polar Science, Polar Research Institute of China, Shanghai, China

33 2 Southern Marine Science and Engineering Guangdong Laboratory (Zhuhai), Zhuhai, Guangdong,

34 China

35 3Department of Geography, Environment and Spatial Sciences, Michigan State University, East

36 Lansing, MI, USA

37 4 National Marine Environmental Forecasting Center, Beijing, China

38

39 *Corresponding Author’s address

40 Dr. Lejiang Yu

41 MNR Key Laboratory for Polar Science, Polar Research Institute of China

42 451 Jinqiao Rd. Shanghai, 200136

43 Phone: 86-21-58712034,

44 Email: yulejiang@sina.com.cn

45

46

47

48

49

50

51 **Abstract.** The recent increasing trend of “warm Arctic, cold continents” has attracted much attention,
52 but it remains debatable as to what forces are behind this phenomenon. Here, we revisited
53 surface-temperature variability over the Arctic and Eurasian continent by applying the
54 Self-Organizing-Map (SOM) technique to gridded daily surface temperature data. Nearly 40% of the
55 surface temperature trends are explained by the nine SOM patterns that depict the switch to the current
56 warm Arctic-cold Eurasia pattern at the beginning of this century from the reversed pattern that
57 dominated the 1980s and the 90s. Further, no cause-effect relationship is found between the Arctic
58 sea-ice loss and the cold spells in high-mid latitude Eurasian continent suggested by earlier studies.
59 Instead, the increasing trend in warm Arctic-cold Eurasia pattern appears to be related to the anomalous
60 atmospheric circulations associated with two Rossby wavetrains triggered by rising sea surface
61 temperature (SST) over the central North Pacific and the North Atlantic Oceans. On interdecadal
62 timescale, the recent increase in the occurrences of the warm Arctic-cold Eurasia pattern is a fragment
63 of the interdecadal variability of SST over the Atlantic Ocean as represented by the Atlantic
64 Multidecadal Oscillations (AMO), and over the central Pacific Ocean.

65

66 **Key words:** Warm Arctic-cold Eurasian continent, Arctic Sea ice, the Kara-Barents Sea, the
67 Self-Organizing-Map (SOM), the Pacific Decadal Oscillation (PDO), the Atlantic Multidecadal
68 Oscillation (AMO)

69

70

71

72

73 1 **Introduction**

74 In recent decades, winter season temperature in the Arctic has been rising at a rate faster than the
75 warming experienced in any other regions of the world (Stroeve et al., 2007; Screen and Simmonds,
76 2010; Stroeve, 2012). In contrasts, there has been an increasing trend in colder than normal winters
77 over the northern mid-latitude continents (Mori et al., 2014; Cohen et al., 2014; 2018). This pattern of
78 opposite winter temperature trend between the Arctic and high-mid latitude continents, referred to as
79 the warm Arctic-cold continents pattern (Overland et al., 2011; Cohen et al., 2014; Walsh, 2014), has
80 received considerable interest in the scientific community especially with regard to dynamical and
81 physical mechanisms for the development of the phenomenon (Mori et al., 2014; Vihma, 2014; Barnes
82 and Screen, 2015; Kug et al., 2015; Overland et al., 2015; Chen et al., 2018).

83 Using observational analyses or coupled ocean-atmosphere modeling, a number of studies have
84 attributed the recent warm Arctic-cold continents pattern to the Arctic sea ice loss in boreal winter
85 (Inoue et al., 2012; Tang et al., 2013; Mori et al., 2014; Kug et al., 2015; Cohen et al., 2018; Mori et al.,
86 2019). Sea ice variability in different parts of the Arctic Ocean has been linked to climate variability in
87 different parts of the world. Specifically, sea ice loss in the Barents and Kara Seas has been linked to
88 cold winters over East Asia (Kim et al., 2014; Mori et al., 2014; Kug et al., 2015; Overland et al., 2015)
89 and in central Eurasia (Mori et al., 2014), while a similar connection has been found between cold
90 winters in North America and sea ice retreat in the East Siberian and Chukchi Seas (Kug et al., 2015).
91 A most recent study (Matsumura and Kosaka, 2019) attributed the warm Arctic-cold continents pattern
92 to the combined effect of Arctic sea ice loss and the atmospheric teleconnection induced by tropical
93 Atlantic sea-surface temperature (SST) anomalies.

94 Other studies, however, found no cause-and-effect relationship between Arctic sea ice loss and

95 mid-latitude climate anomalies (Blackport et al., 2019; Fyfe, 2019). Numerical modeling studies using
96 coupled ocean and atmospheric models simulated no cold mid-latitude winters when the models were
97 forced with reduced Arctic sea ice cover (McCusker et al., 2016; Sun et al., 2016; Koenigk et al., 2019;
98 Blackport et al., 2019; Fyfe, 2019). Instead, these studies pointed to internal atmospheric variability as
99 the likely cause for cold winters in mid-latitudes. Some studies have also suggested that on the
100 interannual timescale mid-latitude atmospheric circulation anomalies triggered by the Pacific and
101 Atlantic SST oscillations may explain both the Arctic sea ice loss and the cooling of the high-mid
102 latitudes (Lee et al., 2011; Luo et al., 2016; Peings et al., 2019; Matsumura and Kosaka, 2019; Clark
103 and Lee, 2019). The sea surface temperature anomalies over the Gulf Stream have also been linked to
104 the Barents Sea ice loss and Eurasian cooling (Sato et al., 2014).

105 Despite the recent attention given to the warm Arctic-cold continents pattern, it remains debatable
106 as to the roles of various dynamical and physical processes play in the formation of this phenomenon.
107 In this study, we revisit surface temperature variability over the Arctic and Eurasia continent (40-90 N,
108 20-130 E), where the warm Arctic-cold continents pattern is a prominent feature (Cohen et al., 2014;
109 Mori et al., 2014), by applying the Self-Organizing-Map (SOM) technique to daily surface temperature
110 over the recent four decades. We will show that while the warm Arctic-cold Eurasian continent pattern
111 has dominated the recent two decades, its opposite pattern, cold Arctic-warm Eurasia continent,
112 appeared frequently in the 1980s and the 90s. Using century-long data, we will further show that the
113 warm Arctic-cold Eurasian continent pattern is an intrinsic climate mode and the recent increasing
114 trend in its occurrence is a reflection of an interdecadal variability of the pattern. Using linear
115 regression, we explain the reason for the recent increasing occurrences of the warm Arctic-cold
116 continents pattern. We also assess the role of the SST anomalies over the North Pacific and Atlantic

117 Oceans in the variability of the warm Arctic-cold Eurasia pattern on the interdecadal time scale.

118 **2 Datasets and methods**

119 2.1 Datasets

120 Daily surface air temperature and other climate variables used in the current analyses, including
121 500 hPa geopotential height, 800-hPa wind and mean sea level pressure, all come from the European
122 Centre for Medium-Range Weather Forecasts Re-Analysis (ERA), the interim version (ERA-Interim;
123 Dee et al., 2011) with a horizontal resolution of approximately 79 km (T255) and 60 vertical levels in
124 the atmosphere. Compared to the earlier versions of ERA (e.g., ERA-40, Uppala et al., 2005) and other
125 global re-analysis products (e.g. the NCEP reanalysis, Kalnay et al., 1996), ERA-Interim has been
126 found to be more accurate in portraying the Arctic warming trend (Dee et al., 2011; Screen and
127 Simmonds, 2011) despite its known warm and moist bias in the surface layer (Jakobson et al., 2012).

128 Daily sea ice data are obtained from the U.S. National Snow and Ice data Center
129 (ftp://sidads.colorado.edu/DATASETS/nsidc0051_gsfc_nasateam_seaice/final-gsfc/north/daily).

130 Gridded monthly SST data used in the current analysis are obtained from the U.S. National Oceanic
131 and Atmospheric Administration (NOAA) data archives
132 (<ftp://ftp.cdc.noaa.gov/Datasets/noaa.oisst.v2.highres/>) (Reynolds et al. 2007). In our analyses, we
133 remain the trends in the data over the 1979-2019 period.

134 The results obtained from the data within the recent four decades are put into the context of the
135 variability over longer time scales using data from the Twentieth Century Reanalysis project, version
136 2C (20CR) that spans more than a century from 1851 through 2015 (Compo et al., 2011). The 20CR
137 reanalysis data, which has a horizontal resolution of 2 °latitude by 2 °longitude and temporal resolution
138 of 6 hours, was produced by a model driven at the lower boundary by observed monthly SST and sea

139 ice conditions and with data assimilation of surface pressure observations. Several indices used to
140 describe known modes of climate variability including Arctic oscillation (AO), Northern Atlantic
141 Oscillation (NAO), Atlantic Multidecadal Oscillation (AMO) (Enfield et al., 2001) and PDO (Mantua
142 et al., 1997), are obtained from NOAA's Climate prediction Center (CPC)
143 (<https://www.esrl.noaa.gov/psd/data/climateindices/list/>),

144 2.2 Methods

145 From the perspective of nonlinear dynamic, a region's climate has its intrinsic modes of variability,
146 but the frequency of occurrence of these internal modes can be modulated by remote forces external to
147 the region (Palmer, 1999l; Hoskins and Woollings, 2015; Shepherd, 2016). In this study we will first
148 obtain the main modes of variability of wintertime surface temperature in a region (40-90 N, 20-130 E)
149 by applying the SOM method (Kohonen, 2001) to daily surface temperature data for the 40 winters
150 (December, January, February) from December 1979 through February 2019. The use of daily data
151 over four decades allows for capturing the variability across two time scales (synoptic and decadal).
152 SOM is a clustering method based on neural network that can transform multi-dimensional data into a
153 two-dimensional array without supervised learning. The array includes a series of nodes arranged by a
154 Sammon map (Sammon, 1969). Each node in the array has a vector that can represent a spatial pattern
155 of the input data. The distance of any two nodes in the Sammon map represents the level of similarity
156 between the spatial patterns of the two nodes. Because SOM has fewer limitations than most other
157 commonly used clustering methods, (e.g., orthogonality required by the empirical orthogonal function
158 or EOF method), the SOM method can describe better the main variability patterns of the input data
159 (Reusch et al., 2005).

160 SOM method has been used in atmospheric research at mid and high latitudes of the northern

161 hemisphere (Skific et al., 2009; Johnson and Feldstein, 2010; Horton et al., 2015; Loikith and Broccoli,
162 2015; Vihma et al., 2019). For example, Johnson and Feldstein (2010) used SOM to identify spatial
163 patterns of daily wintertime North Pacific sea level pressure and relate the variability of the
164 occurrences of those patterns to some large-scale circulation indices. Loikith and Broccoli (2015)
165 compared observed and model-simulated circulation patterns across the North American domain using
166 an approach involving SOM. The SOM method was also used to detect circulation pattern trends in
167 a subset of North America during two different periods (Horton et al., 2015).

168 In this study, the SOM method is applied to ERA-Interim wintertime daily temperature anomalies from
169 December 1979 through February 2019. The anomalies are calculated by subtracting 40-year averaged
170 daily temperature from the original daily temperature at each grid point. Prior to SOM analysis, it is
171 necessary to determine how many SOM nodes are needed to best capture the variability in the data.
172 According to previous studies (Lee and Feldstein, 2013; Gibson et al., 2017; Schudeboom et al., 2018),
173 the rule for determining the number of SOM nodes is that the number should be sufficiently large to
174 capture the variability of the data analyzed, but not too large to introduce unimportant details. Table 1
175 shows the averaged spatial correlation between all daily surface air temperature anomalies and their
176 matching nodes. The spatial correlation coefficients increase from 0.26 for a 3×1 grid to 0.51 for a
177 4×4 grid, but the gain from a 3×3 grid to a 4×4 grid is relatively small. Hence, a 3×3 grid seems to
178 meet the above-mentioned rule and will be utilized in this study.

179 The contribution of each SOM node to the trend in wintertime surface temperature anomalies is
180 calculated by the product of each node pattern and its frequency trend normalized by the total number
181 (90) of wintertime days (Lee and Feldstein, 2013). The sum of the contributions from all nodes denotes
182 the SOM-explained trends. Residual trends are equal to the subtraction of SOM-explained trends from

183 the total trends. The anomalous atmospheric circulation pattern corresponding to each of the SOM
184 pattern is obtained by composite analysis that computes a composite mean of an atmospheric
185 circulation field (e.g., 500 hPa height) over all occurrences of that SOM node. Regression analysis is
186 also performed where atmospheric circulation variables are regressed onto the time series of the
187 occurrence of a SOM node to further elucidate the relationship between the variability of atmospheric
188 circulations and surface temperatures. The statistical significance of composite and regression analyses
189 in this study is tested by using the Student's t test.

190 **3 Results**

191 **3.1 Surface temperature variability**

192 The majority of the 9 SOM nodes depict a dipole pattern characterized by opposite changes in
193 surface temperatures between the Arctic Ocean and the Eurasian continent, although the sign switch
194 does not always occur at the continent-ocean boundary (Figure 1). The differences in the position of the
195 boundary between the warm and cold anomalies reflects the transition between the cold Arctic-warm
196 Eurasia pattern (denoted, in descent order of the occurrence frequency, by nodes 3, 9, 6), to the warm
197 Arctic-cold Eurasia pattern (depicted, in descent order of the occurrence frequency, by nodes 1, 7, 4).
198 The spatial patterns represented by the first group of nodes are almost mirror images of the patterns
199 denoted by the corresponding nodes in the second group. For example, the second node in group 1
200 (node 9, 15.4%) and the first node in group 2 (node 1, 17.1%) show a mirror image pattern with cold
201 (warm) anomalies in the Arctic Ocean extending into northern Eurasia and warm (cold) anomalies in
202 the rest of the Eurasia continent in the study domain. In both cases, the region of maximum magnitude
203 anomalies is centered near Svalbard, Norway. The second pair, denoted by node 3 (17.2%) and 7
204 (13.7%) has the boundary of separation moved northward from northern Eurasia continent toward the

205 shore of the Arctic Ocean. While the maximum anomaly in the Arctic Ocean remains close to Svalbard,
206 maximum values over the continent are found in central Russia. Nodes 4-6 display a noticeable
207 transition from node 1 to node 7 and from node 3 to node 9, respectively. Although nodes 2 and 8 show
208 an approximate monopole spatial pattern, they also represent a transition between nodes 1 and 3, and
209 between nodes 7 and 9, respectively. Above SOM analysis does not consider the trend in surface air
210 temperature. The result is similar when the trend is removed (not shown).

211 The temporal variability on this time scale is typically related to synoptic processes and hence the
212 questions are what synoptic patterns are responsible for the occurrence of the spatial patterns depicted
213 by each of the 9 SOM nodes and how these patterns are related to those of the Arctic sea ice anomalies?
214 These questions can be answered by using the composite method. Specifically, for each SOM node,
215 composite maps are made respectively for the anomalous 500-hPa geopotential height, mean sea level
216 pressure, 850-hPa wind, downward longwave radiation, surface turbulent heat flux, and sea ice
217 concentration over all the days when the spatial variability of the surface temperature anomalies is best
218 matched by the spatial pattern of that node.

219 3.2 Large-scale circulation patterns

220 For all SOM nodes, the spatial pattern of the composited 500-hPa geopotential height anomalies
221 (Figure 2) is similar to that of mean sea level pressure anomalies (not shown), indicating an
222 approximately barotropic structure. For nodes 1, 4 and 7, the 500-hPa height anomalies show a dipole
223 structure of positive values over Siberia and negative values to its south over the Eurasian continent.
224 Anomalous southwesterly winds on the western side of the anticyclone over Siberia transport warm
225 and moist air from northern Europe and the North Atlantic Ocean into the Atlantic sector of the Arctic
226 Ocean (Figure 3), providing a plausible explanation of the warm surface temperature anomalies in the

227 region (Figure 1). On the eastern side of the anticyclone, anomalous northwesterly winds bring cold
228 and dry air from the Arctic Ocean into Eurasia continent, which is consistent with the negative surface
229 temperature anomalies there. The opposite occurs for nodes 3, 6 and 9. A similar explanation involving
230 anomalous pressure and wind fields can be applied to other nodes. The dipole structure that dominates
231 the anomalous 500-hPa height fields over the North Atlantic Ocean for most nodes resembles the
232 spatial pattern of the NAO (Figure 2). In addition, the patterns for several nodes, such as nodes 4 and 7,
233 have some resemblance to the spatial pattern of the AO over larger geographical region. The possible
234 connection to NAO and AO is further investigated by averaging the daily index values of NAO or AO
235 over all occurrence days for each node. The results (Table 2) show that nodes 1, 2, 3 (5, 8, 9)
236 correspond to a significant positive (negative) phase of the NAO index characterized by negative
237 (positive) height anomalies over Iceland and positive (negative) values over the central North Atlantic
238 Ocean. Association is also found between nodes 1, 2, 3, and 6 (5, 7, 8, and 9) and the positive (negative)
239 phases of the AO index.

240 3.3 Downward radiative fluxes

241 Besides the anomalous circulation patterns, anomalous surface radiative fluxes may also play a role in
242 shaping the spatial pattern of surface temperature variability. In fact, the spatial pattern of the mean
243 anomalous daily downward longwave radiation for an individual node (Figure 4) is in good agreement
244 with the spatial pattern of the surface temperature anomalies of that node. In other words, increased
245 downward longwave radiation is associated with positive surface temperature anomalies, and vice
246 versa. As expected from previous studies (e.g., Sedlar et al. 2011), there is a significant positive
247 correlation between downward longwave radiative fluxes and the anomalous total column water vapor
248 and mid-level cloud cover (not shown). The correlation to low- and high-level cloud cover is, however,

249 not significant (not shown). Most of the water vapor in both the Arctic and Eurasia is derived from the
250 North Atlantic Ocean, but the water vapor is transported into the Arctic by southwesterly flows and into
251 Eurasia by northwesterly winds. The anomalous shortwave radiation corresponding to each node (not
252 shown) is an order of magnitude smaller than of the longwave radiation anomalies and has a spatial
253 pattern opposite to that of the mid-level cloud cover and the longwave radiation anomalies.

254 3.4 Sea ice

255 The analyses presented above attempt to explain the spatial pattern of surface temperature
256 variability for each node from the perspective of anomalous heat advection and surface radiative fluxes.

257 As mentioned earlier, there has been a debate in the literature about the role played by the sea ice
258 anomalies in the Barents and Kara Seas in the development of the warm Arctic-cold Eurasia pattern.

259 Here, we examine the anomalous turbulent heat flux (Figure 5) and sea ice concentration (Figure 6) for
260 each node. Turbulent heat flux is considered positive when it is directed from the atmosphere
261 downward to the ocean or land surfaces. Thus, a positive anomaly indicates either an increase in the
262 atmosphere-to-surface heat transfer or a decrease in the heat transfer from the surface to the atmosphere.

263 The magnitude of anomalous turbulent heat flux is found to be comparable to that of anomalous
264 downward longwave radiation (Figure 4). For all nodes, the heat flux anomalies are larger over ocean
265 than over land (Figure 5). For node 1, positive turbulent heat flux anomalies occur mainly over the

266 Barents Sea, the western and central North Atlantic Ocean and the eastern North Pacific Ocean,
267 indicating an increase in heat transport from the air to the ocean due possibly to an increase in vertical

268 temperature gradient caused by warm air advection associated with anomalous circulation (Figures 2
269 and 3). The downward heat transfer results in sea ice melt in the Greenland Sea and the Barents Sea

270 (Figure 6). For node 4, the anomalous southerly winds over the Nordic Sea produce larger positive

271 turbulent heat flux anomalies (Figure 5). For node 7, the anticyclone is located more northwards, which
272 generates opposite anomalous winds between the Nordic and northern Barents Seas and the southern
273 Barents Sea and thus opposite turbulent heat flux anomalies that are consistent with the opposite sea ice
274 concentration anomalies in the two regions (Figure 5). For nodes 3, 6, and 9, the anomalous cold air
275 from the central Arctic Ocean flows into warm water in the Nordic and Barents Seas, producing
276 negative turbulent heat flux anomalies and positive sea ice concentration anomalies (Figures 5 and 6).
277 Sorokina et al. (2016) noted that turbulent heat flux usually peaks 2 days before changes in surface
278 temperature pattern occur. The pattern of the composited anomalous 500-hPa geopotential height,
279 turbulent heat flux and sea ice concentration 2 days prior to the day when the nodes occur (not shown)
280 is similar to the current-day pattern in Figures 2, 5, and 6. Our results support the conclusion of
281 Sorokina et al. (2016) and Blackport et al. (2019) that the anomalous atmospheric circulations lead to
282 the anomalous sea ice concentration in the Barents Sea.

283 3.5 Trends in wintertime surface temperature

284 The results above suggest that both the surface temperature anomaly patterns over the Arctic Ocean
285 and Eurasian continent and the sea ice concentration anomalies in the Nordic and Barents Seas can be
286 explained largely by changes in atmospheric circulations and the associated vertical and horizontal heat
287 and moisture transfer by mean and turbulent flows. Next, we assess the trends of wintertime surface
288 temperature and the contributions of the SOM nodes to the trends.

289 We first examine the time series of the accumulated number of days for each node in each winter
290 for the 1979-2019 period (Figure 7). The time series for nodes 1, 4, 6, and 9 exhibit variability on
291 interannual as well as decadal time scales. The occurrence frequency is noticeably larger after 2003
292 than prior to 2003 for nodes 1 and 4, and vice versa for nodes 6 and 9, and the difference between the

293 two periods is significant at 95% confidence level. Given the spatial patterns of these four nodes
294 (Figure 1), this indicates that the warm Arctic-cold Eurasia pattern occurred more frequently after 2003.
295 A linear trend analysis of the time series for each node (Table 3) reveals significant positive trends in
296 occurrence frequency for nodes 1 and 4 and significant negative trends for nodes 6 and 9, which agree
297 with the result from a previous study (Clark and Lee, 2019; Overland et al., 2015) that suggested an
298 increasing trend of the warm Arctic and cold Eurasia pattern.

299 These trends in the occurrence frequency of the SOM nodes contribute to the trends in the total
300 wintertime (DJF) surface temperature anomalies (Figure 8, top panel) that have significant positive
301 trends over the Arctic Ocean and in regions of Northern and Eastern Europe and negative, mostly
302 insignificant trends in Central Siberia. The contribution, however, varies from node to node (Figure 9).
303 Node 1 has the largest domain-averaged contribution of 18.7%, followed by its mirror node (node 9) at
304 10.1%. Nodes 4 and 6 account for 2.8% and 4.3% of the total trend, respectively. None of the
305 remaining nodes explain more than 2%. All nodes together explain 39.5% of the total trend in
306 wintertime surface air temperature. The spatial pattern of the SOM-explained trends (Figure 8, middle
307 panel) is similar to the warm Arctic-cold continent pattern, whereas the residual trend resembles more
308 the total trend (Figure 8 bottom panel).

309 3.6 Mechanisms

310 The results presented above indicate that the SOM patterns explain nearly 40% of the trend in
311 wintertime surface air temperature anomalies and majority of the contributions (35 out of 40%) come
312 from the two pairs of the nodes (nodes 1, 9, and 4, 6). The analyses hereafter will focus on these four
313 nodes. Below we assess the atmospheric and oceanic conditions associated with the occurrences of the
314 four nodes via regression analysis. Specifically, the anomalous seasonal SST and atmospheric

315 circulation variables are regressed onto the normalized time series of the number of days when each of
316 the four nodes occurs (Figures 10, 11, and 12).

317 For node 1, the SST regression pattern in the Pacific Ocean shows significant positive anomalies
318 over the tropical western Pacific Ocean and central North Pacific Ocean (Figure 10). The positive SST
319 anomalies also occur over most of the North Atlantic. Negative SST anomalies occur over the central
320 tropical Pacific Ocean, though they are not significant at 95% confidence level. The SST regression
321 pattern is reversed for node 9. The direction of wave activity flux indicates the direction of group speed
322 of stationary planetary wave. Here we calculate the wave activity flux defined by Takaya and
323 Nakamura (2001), which considers the influence of mid-latitude zonal wind (Figure 12). For node 1,
324 the corresponding anomalous 500-hPa height regression (Figure 11) shows two Rossby wavetrains: one
325 is excited over the central Pacific Ocean and propagates northeastwards into North America and North
326 Atlantic Ocean, and the other, which displays a stronger signal, originates from central North Atlantic
327 and propagates northeastwards to the Arctic Ocean and southeastwards to the Eurasian continent
328 (Figure 11 and 12). For node 9, the corresponding anomalous 500-hPa height and streamfunction show
329 an opposite pattern, but the wave activity flux is similar to that of node 1.

330 For node 4, the SST anomalies over the tropical Pacific Ocean appear to be in a La Niña state,
331 which shows stronger negative SST anomalies over the eastern tropical Pacific Ocean than those for
332 node 1 (Figure 10). The positive SST anomalies over the North Pacific shift more northwards relative
333 to that of node 1. The positive SST anomalies over the North Atlantic are weaker than those for node 1.
334 The corresponding wavetrain over the Pacific Ocean is stronger than that over the Atlantic Ocean
335 (Figure 11), which is also be observed in the pattern of wave activity and streamfunction (Figure 12).
336 The corresponding pattern for node 6 is nearly reversed, but there are some noticeable differences in

337 the amplitude of the wavetrain and SST anomalies. For example, the magnitude of the anomalous SST
338 and the 500-hPa height over the central North Pacific is larger for node 6 than that for node 4.

339 Besides the above-mentioned variables, similar regression analysis is also performed for the
340 anomalous 850-hPa wind field and anomalous downward longwave radiation (not shown). Their
341 regression patterns, which are similar to those in Figures 3 and 4, explain well the decadal variability of
342 the number of days for nodes 1, 4, 6, and 9. Together, these results in Figures 10-12 indicate that the
343 decadal variability of the occurrence frequency of the four nodes in recent decades is related to two
344 wavetrains induced by SST anomalies over the central North Pacific Ocean and the North Atlantic
345 Ocean (Figures 10 and 11). The aforementioned SST regression patterns over the Atlantic and Pacific
346 Oceans also show features of the AMO and PDO (Figure 10). Since both the AMO and PDO exhibited
347 a phase change in the late 1990s (Yu et al., 2017), the question is whether a similar change in the SOM
348 frequency also appear in the late 1990s. A comparison of the averaged frequency before and after 1998
349 shows a significant drop in frequency for nodes 6 and 9 and an increase in frequency for node 1 (not
350 shown). This result suggests that the change in the AMO and PDO indices may contribute to the change
351 in the frequencies of the warm Arctic-cold Eurasia continent pattern.

352 3.7 Interdecadal variability

353 The four-decade-long ERA-Interim reanalysis is not adequate for examining interdecadal to
354 multi-decadal variations represented by the PDO and AMO indices. Further analysis is performed using
355 the 20CR daily reanalysis data for the 1854-2014 period. Before applying the SOM technique to the
356 20CR data, we first remove the trend to eliminate the influence from the global warming. No low-pass
357 filter is applied before SOM analysis in order to test the stability of the SOM results for the different
358 periods. The spatial SOM patterns from the de-trended century-long 20CR data (Figure 13) are similar

359 to those for the 1979-2019 period (Figure 1). Nodes 1, 4, and 7 correspond to the positive phase of the
360 warm Arctic-cold Eurasia pattern and the negative phase can be observed in nodes 3, 6, and 9. The
361 magnitude in Figure 13 is smaller compared to the recent four decades in Figure 1. The occurrence
362 frequencies of the four nodes, 1, 4, 6, and 9 (Figure 14), are close to those for the recent four decades
363 (Figure 7). It indicates that the SOM method can obtain stably the main modes of wintertime surface
364 air temperature variability. For the recent four decades, the time series of the number of days also
365 displays a noticeable increasing (decreasing) trend for nodes 1 and 4 (6 and 9), suggesting that the
366 trend in the recent four decades is a reflection of an interdecadal variability of wintertime surface air
367 temperature.

368 Next, we apply a 40-year low-pass filter to the time series of the occurrence frequencies for nodes
369 1, 4, 6 and 9 and the AMO and PDO indices and calculate correlations. There is a significant
370 correlation between the time series and the AMO index, with correlation coefficients of 0.36 for node 1,
371 0.27 for node 4, -0.37 for node 6, and -0.20 for node 9, all of which are at the 95% confidence level. No
372 significant correlations, however, are found between the filtered time series and the PDO index. If we
373 define a SST index to represent the variability of SST anomalies over the central North Pacific Ocean
374 (20°N-40°N, 150°E-150°W), the 40-year low-pass filtered central North Pacific Ocean SST index is
375 now significantly correlated with the filtered time series of occurrence frequencies for nodes 1 and 9
376 (0.55 for node 1 and -0.46 for node 9). The correlation results are consistent with the SST regression
377 map for the recent decades (Figure 10).

378 To confirm the effect of SST anomalies on the warm Arctic -cold Eurasia pattern, we also perform
379 EOF analysis of wintertime detrended seasonal surface air temperature anomalies for the 1854-2014
380 period (Figure 15). The spatial patterns of the first and second EOF modes show the negative phase of

381 the warm Arctic-cold Eurasia pattern and the 40-year low-pass filtered time series is inversely
382 correlated with the 40-year low-pass filtered wintertime AMO index (-0.46, $p<0.05$ for mode 1 and
383 -0.44, $p<0.05$ for mode 2). The 40-year low-pass filtered time series of the two EOF modes have a
384 significant negative correlation with the 40-year low-pass filtered central North Pacific Ocean SST
385 index, with correlation coefficients of -0.19 and -0.26 ($p<0.05$). Only PC1 has a significant correlation
386 with the PDO index (0.38, $p<0.05$). Thus, the increase in the occurrence of the warm Arctic-cold
387 Eurasia pattern in the recent decades is a part of the interdecadal variability of the pattern, which is
388 influenced by the AMO index, the PDO index, and the central North Pacific SST.

389 **4 Conclusions and Discussions**

390 In this study, we examine the variability of wintertime surface air temperature in the Arctic and the
391 Eurasian continent (20°E-130°E) by applying the SOM method to daily temperature from the gridded
392 ERA-Interim dataset for the period 1979-2019 and from the 20CR reanalysis for the period 1854-2014
393 and the EOF method to seasonal temperature from the 20CR reanalysis for the period 1854-2014. The
394 spatial pattern in the surface temperature variations in the study region, as revealed by the nine SOM
395 nodes, is dominated by concurrent warming in the Arctic and cooling in Eurasia, and vice versa. The
396 nine SOM patterns explain nearly 40% of the trends in wintertime surface temperature and 88% of that
397 are accounted for by only four nodes. Two of the four nodes (nodes 1 and 4) represent the warm
398 Arctic-cold Eurasian pattern and the other two (nodes 6 and 9) depict the opposite cold Arctic-warm
399 Eurasia pattern. There is a clear shift in the frequency of the occurrence of these patterns near the
400 beginning of this century, with the warm Arctic – cold Eurasia pattern dominating since 2003, while the
401 opposite pattern prevailing from the 1980s through the 1990s. The warm Arctic-cold Eurasia pattern is
402 accompanied by an anomalous high pressure and anticyclonic circulation over the Eurasian continent.

403 The anomalous winds and the associated temperature and moisture advection interact with local
404 longwave radiative forcing and turbulent fluxes to produce positive (negative) temperature anomalies
405 in the Arctic (Eurasian continent). The circulation is reversed for the cold Arctic-warm Eurasia pattern.
406 The warm, moist air mass is advected to the Arctic by the anomalous atmospheric circulations and the
407 increased downward turbulent heat flux also explain sea ice melt in the Barents and Kara Seas. In other
408 words, the sea ice loss in the Barents and Kara Seas and the cooling of the Eurasian continent can both
409 be traced to anomalous atmospheric circulations.

410 Increasing occurrences of the warm Arctic-cold Eurasian continent pattern appear to relate to
411 rising SST over the central North Pacific and North Atlantic Oceans (positive AMO phase). The SST
412 anomalies trigger two Rossby wavetrains spanning from the North Pacific Ocean, North America, and
413 the North Atlantic Ocean to the Eurasian continent. The two wavetrains are strengthened through local
414 sea-atmosphere-ice interactions in mid-high latitudes, which influence the change in the occurrence
415 frequency of the warm Arctic-cold Eurasian continent pattern. Our results agree with those of previous
416 studies (Lee et al., 2011; Sato et al., 2014; Clark and Lee, 2019). But previous studies only focus on the
417 effects of SST anomalies over either North Pacific or North Atlantic Oceans. We also note that the two
418 wavetrains excited by SST anomalies over different oceans differ in amplitudes, leading to somewhat
419 different warm Arctic-cold Eurasia patterns.

420 Using century-long data, we show that the warm Arctic-cold Eurasia pattern is an intrinsic climate
421 mode, which has been stable since 1854. The recent increasing trend in its occurrence is a reflection of
422 an interdecadal variability of the pattern resulting from the interdecadal variability of SST anomalies
423 over the central Pacific Ocean and over the Atlantic Ocean represented by the AMO index. Sung et al.
424 (2018) investigated interdecadal variability of the warm Arctic and cold Eurasia pattern and considered

425 the variability of the SST over the North Atlantic as its origin. Our results suggest that the variability of
426 the SST over the North Pacific also plays an important role. However, internal atmospheric variability
427 remains another potential source. The Rossby wavetrains also lead to deepening of a trough in East
428 Asia and generate an anomalous low pressure and cold temperature in northern China (Figure 10),
429 which further suggests that a warmer Arctic, especially warmer Barents and Kara Seas is not the driver
430 for the increasing occurrence of cold spells in East Asia, as suggested in previous studies (Kim et al.,
431 2014; Mori et al., 2014; Kug et al., 2015; Overland et al., 2015).

432 Our results suggest that the increasing trend in warm Arctic-cold Eurasia pattern may be related to
433 the anomalous SST over the central North Pacific and the North Atlantic Oceans. But we cannot rule
434 out the influence of the Arctic sea ice loss on the trend. The Arctic sea ice loss results from both Arctic
435 warming due to anthropogenic increasing of greenhouse gas concentrations and natural variability of
436 climate system such as SST anomalies. This study considers natural variability or internal driver of
437 climate system. The Arctic warming caused external forcing related to increasing greenhouse gas
438 emissions can produce an anomalous anticyclone over the Barents and Kara Seas, leading to the warm
439 Arctic-cold continents pattern.

440 Although the ERA-Interim reanalysis is overall superior in describing the Arctic atmospheric
441 environment to other similar global reanalysis products, it contains warm and moist biases in the
442 surface layer (Jakobson et al., 2012; Chaudhuri et al., 2014; Simmons and Poli, 2015; Wang et al.,
443 2019). However, we believe these biases, as well as the relatively coarse resolution, should have
444 minimum impact in the results from the current analyses. Further, although the current analyses were
445 performed on a predetermined SOM grid with 3x3 nodes, an increase in the number of SOM nodes
446 didn't change the conclusions.

447 Our results help broaden the current understanding of the formation mechanisms for the warm
448 Arctic-cold Eurasia pattern. The SST anomalies over Northern Hemisphere oceans may offer a
449 potential for predicting its occurrence. The statistical relationship between SST anomalies and the
450 occurrences of the warm Arctic-cold continents pattern may help improve the predictability of
451 wintertime surface air temperature over Eurasian continent on interdecadal time scales.

452 **Data Availability**

453 All data used in the current analyses are publicly available. The monthly sea ice concentration data are
454 available from the National Snow and Ice Data Center (NSIDC) (<http://nsidc.org/data/NSIDC-0051>), the
455 ERA-Interim reanalysis data are available from the European Center for Mid-Range Weather
456 Forecasting (<https://www.ecmwf.int/en/forecasts/datasets/reanalysis-datasets/era-interim>) and the sea
457 surface temperature data are available from the Hadley Centre for Climate Prediction and Research
458 (<ftp://ftp.cdc.noaa.gov/Datasets/noaa.oisst.v2.highres/>). The long-term SST data are derived from
459 from the Twentieth Century Reanalysis project, version 2c (20CR)
460 (<https://climatedataguide.ucar.edu/climate-data/noaa-20th-century-reanalysis-version-2-and-2c>).

461 **Competing interests**

462 The authors declare that they have no conflict of interest.

463 **Author Contributions**

464 L. Yu designed the study, with input from S. Zhong, and carried out the analyses. L. Yu and S. Zhong
465 prepared the manuscript. C. Sui plotted a part of Figures. B. Sun revised the manuscript.

466 **Acknowledgements** We thank the European Centre for Medium-Range Weather Forecasts (ECMWF)
467 for the ERA-Interim data. This study is financially supported by the National Key R&D Program of
468 China (2019YFC1509102; 2017YFE0111700) and the National Natural Science Foundation of China
469 (41922044).

470

471

472

473 **References**

474 Barnes, E. A. and Screen, J. A.: The impact of Arctic warming on the midlatitude jet-stream: Can it?
475 Has it? Will it?, WIRES Clim. Change, 6, 277-286, doi:10.1002/wcc.337, 2015.

476 Blackport, R., Screen J. A., Wiel K. van der, and Bintanja, R.: Minimal influence of reduced Arctic sea
477 ice on coincident cold winters in mid-latitudes, Nature Climate Change, 9,
478 doi:10.1038/s41558-019-0551-4, 2019, 2019.

479 Chaudhuri, A. H., Ponte, R. M., and Nguyen, A. T.: A Comparison of atmospheric reanalysis products
480 for the Arctic Ocean and implications for uncertainties in air-sea fluxes, J. Climate, 27,
481 5411-5421, doi:10.1175/JCLI-D-13-00424.1, 2014.

482 Chen, L., Francis J. and Hanna E.: The “Warm-Arctic/Cold continents” pattern during 1901-2010, Int. J.
483 Climatol., 38, 5245-5254, [doi:10.1002/joc.5725](https://doi.org/10.1002/joc.5725), 2018.

484 Clark, J. P. and Lee, S.: The role of the tropically excited Arctic Warming Mechanism on the warm
485 Arctic cold continent surface air temperature trend pattern, Geophys. Res. Lett., 46, 8490-8499,
486 doi:10.1029/2019GL082714, 2019

487 Cohen, J., Screen, J. A., Furtado, J. C., Barlow, M., Whittleston, D., Coumou, D., Francis, J., Dethloff,
488 K., Entekhabi, D., Overland, J., and Jones, J.: Recent Arctic amplification and extreme
489 mid-latitude weather, Nat. Geosci., 7, 627-637, doi:10.1038/ngeo2234, 2014.

490 Cohen, J., Pfeiffer, K., and Francis, J. A.: Warm Arctic episodes linked with increased frequency of
491 extreme winter weather in the United States, Nat. Commun., 9, 869,
492 doi:10.1038/s41467-018-02992-9, 2018.

493 Compo, G. P., Whitaker, J. S., Sardeshmukh, P. D., Matsui, N., Allan, R., Yin, X., Jr, G. B. E., Vose, R.

494 S., Rutledge, G. K., Bessemoulin, P., Brönnimann, S., Brunet, M., Crouthamel, R. I., Grant, A.

495 N., Groisman, P. Y., Jones, P. D., Kruk, M. C., Kruger, A. C., Marshall, G. J., Maugeri, M., Mok,

496 H. Y., Nordli, Ø., Ross, T. F., Trigo, R. M., Wang, X., Woodruff, S. D., and Worley S. J.: The

497 Twentieth Century Reanalysis Project, *Quart. J. Roy. Meteor. Soc.*, 137, 1-28,

498 doi:10.1002/qj.776, 2011.

499 Dee, D. P., Uppala, S. M., Simmons, A. J., Berrisford, P., Poli, P., Kobayashi, S., Andrac, U.,

500 Balmaseda, M. A., Balsamo, G., Bauer, P., Bechtold, P., Beljaars, A. C. M., van de Berg, L.,

501 Bidlot, J., Bormann, N., Delsol, C., Dragani, R., Fuentes, M., Geer, A. J., Haimberger, L., Healy,

502 S. B., Hersbach, H., Hólm, E. V., Isaksen, L., Källberg, P., Köhler, Matricardi, M., McNally, A.

503 P., Monge-Sanz, B. M., Morcrette, J.-J., Park, B.-K., Peubey, C., de Rosnay, P., Tavolato, C.,

504 Thépaut, J.-N., and Vitart, F.: The ERA-Interim reanalysis: configuration and performance of the

505 data assimilation system, *Q. J. R. Meteorol. Soc.*, 137, 553-597, doi:10.1002/qj.828, 2011.

506 Enfield, D. B., Mestas-Nunez, A. M., and Trimble, P. J.: The Atlantic multidecadal oscillation and its

507 relation to rainfall and river flows in the continental U.S., *Geophys. Res. Lett.*, 28, 2077-2080,

508 2001.

509 Fyfe, J. C.: Midlatitudes unaffected by sea ice loss, *Nature Climate Change*, 9,

510 doi:10.1038/s41558-019-0560-3, 2019 .

511 Gibson, P. B., Perkins-Kirkpatrick, S. E., Uotila, P., Pepler, A. S., and Alexander, L. V.: On the use of

512 self-organizing maps for studying climate extremes, *J. Geophys. Res. Atmos.*, 122, 3891–3903,

513 doi:10.1002/2016JD026256, 2017.

514 Hoskins, B. and Woollings, T.: Persistent extratropical regimes and climate extremes, *Curr. Clim. Change*

515 Rep., 1, 115-124, doi:10.1007/s40641-015-0020-8, 2015

516 Horton, D. E., Johnson, N. C., Singh, D., Swain, D. L., Rajaratnam, B., and Diffenbaugh, N. S.:
517 Contribution of changes in atmospheric circulation patterns to extreme trends, *Nature*,
518 522,465-469, doi:10.1038/nature14550, 2015.

519 Inoue, J., Hori, M. E., and Takaya, K.: The role of Barents Sea ice in the wintertime cyclone track and
520 emergence of a warm-Arctic-Siberian anomaly, *J. Clim.*, 25, 2561-2568,
521 doi:10.1175/JCLI-D-11-00449.1, 2012.

522 Jakobson, E., Vihma, T., Palo, T., Jakobson, L., Keernik, H., and Jaagus, J.: Validation of atmospheric
523 reanalyses over the central Arctic Ocean, *Geophys. Res. Lett.*, 39, L10802,
524 doi:10.1029/2012GL051591, 2012.

525 Johnson, N. C. and Feldstein, S. B.: The continuum of North Pacific sea level pressure patterns:
526 Intraseasonal, interannual, and interdecadal variability, *J. Clim.*, 23,
527 851-867, doi:10.1175/2009JCLI3099.1, 2010.

528 Jakobson, E., Vihma, T., Palo, T., Jakobson, L., Keernik, H., Jaagus, J.: Validation of atmospheric
529 reanalyses over the central Arctic Ocean, *Geophys. Res. Lett.*, 39, 2012.

530 Kalnay, E., Kanamitsu, M., Kistler, R., Collins, W. G., Deaven, D., Gandin, L., Iredell, M., Saha, S.,
531 White, G., Woollen J.: The NCEP/NCAR 40-year reanalysis project, *Bull. Amer. Meteor. Soc.*,
532 77, 437-471, doi:10.1175/1520-0477(1996)077<0437:TNYRP>2.0.CO;2, 1996.

533 Kim, B.-M., Son, S.-W., Min, S.-K., Jeong, J.-H., Kim, S.-J., Zhang, X., Shim, T., and Yoon, J.-H.:
534 Weakening of the stratospheric polar vortex by Arctic sea-ice loss, *Nature Commun.*, 5, 4646,
535 doi:10.1038/ncomms5646, 2014.

536 Kohonen, T.: *Self-Organizing Maps*. 3rd ed. Springer, 501 pp, 2001.

537 Kug, J.-S., Jeong, J.-H., Jang, Y.-S., Kim, B.-M., Folland, C. K., Min, S.-K., and Son, S.-W.: Two

538 distinct influeunces of Arctic warming on cold winters over North America and East Asia, *Nat.*
539 *Geosci.*, 8, 759-762, doi:10.1038/ngeo2517, 2015.

540 Lee, S., Gong, T., Johnson, N., Feldstein, S. B., and Polland, D.: On the possible link between tropical
541 convection and the Northern Hemisphere Arctic surface air temperature change between 1958
542 and 2001, *J. Clim.*, 24, 4350-4367, doi:10.1175/2011JCLI4003.1, 2011.

543 Lee, S. and Feldstein, S. B.: Detecting ozone- and greenhouse gas–driven wind trends with
544 observational data, *Science*, 339, 563–567, [doi:10.1126/science.1225154](https://doi.org/10.1126/science.1225154), 2013.

545 Loikith, P. C. and Broccoli, A. J.: Comparison between observed and model-simulated atmospheric
546 circulation patterns associated with extreme temperature days over North America using CMIP5
547 historical simulations, *J. Clim.*, 28, 2063-2079, doi:10.1175/JCLI-D-13-00544.1, 2015.

548 Luo, D., Xiao, Y., Yao, Y., Dai, A., Simmonds, I., and Franzke, C. L. E.: Impact of Ural blocking on
549 winter warm Arctic-cold Eurasian anomalies. Part I: Blocking-induced amplification, *J. Clim.*,
550 29, 3925-3947, doi:10.1175/JCLI-D-15-0611.1, 2016.

551 Mantua, N. J., Hare, S. R., Zhang, Y., Wallace, J. M., and Francis, R. C.: A Pacific interdecadal climate
552 oscillation with impacts on salmon production, *Bull. Amer. Meteor. Soc.*, 78, 1069–1079, 1997.

553 Matsumura, S. and Kosaka, Y.: Arctic-Eurasian climate linkage induced by tropical ocean variability,
554 *Nature Communications*, 10, 3441, doi:10.1038/s41467-019-11359-7, 2019.

555 Mori, M., Watanabe, M., Shiogama, H., Inoue, J., and Kimoto, M.: Robust Arctic sea-ice influence on
556 the frequent Eurasian cold winters in past decades, *Nat. Geosci.*, 7, 869-873,
557 doi:10.1038/ngeo2277, 2014.

558 Mori, M., Kosaka, Y., Watanabe, M., Nakamura, H., and Kimoto, M.: A reconciled estimate of the
559 influence of Arctic sea-ice loss on recent Eurasian cooling, *Nat. Clim. Change*, 9, 123-129,

560 doi:10.1038/s41558-018-0379-3, 2019.

561 McCusker, K. E., Fyfe, J. C., and Sigmond, M.: Twenty-five winters of unexcepted Eurasian cooling

562 unlikely due to Arctic sea-ice loss, *Nat. Geosci.*, 9, 838-842, doi:10.1038/ngeo2820, 2016.

563 Overland, J. E., Wood, K. R., and Wang, M.: Warm Arctic-cold continents: climate impacts of the

564 newly open Arctic sea, *Polar Res.*, 30, 15787, doi:10.3402/polar.v30i0.15787, 2011.

565 Overland, J. E., Francis, J., Hall, R., Hanna, E., Kim, S.-J., and Vihma, T.: The melting Arctic and

566 Midlatitude weather patterns: Are they connected?, *J. Clim.*, 28, 7917-7932,

567 doi:10.1175/JCLI-D-14-00822.1, 2015.

568 Palmer, T. N.: A nonlinear dynamical perspective on climate prediction, *J. Clim.*, 12, 575-591, 1999.

569 doi:10.1175/1520-0442(1999)012<0575:ANDPOC>2.0.CO;2

570 Peings, Y.: Ural blocking as a driver of early-winter stratospheric warmings, *Geophys. Res. Lett.*, 46,

571 5460-5468, doi:10.1029/2019GL082097, 2019.

572 Reusch, D. B., Alley, R. B., and Hewitson, B. C.: Relative performance of self-organizing maps and

573 principal component analysis in pattern extraction from synthetic climatological data, *Polar*

574 *Geogr.*, 29, 188–212, doi:10.1080/789610199, 2005.

575 Reynolds, R. W., Smith, T. M., Liu, C., Chelton, D. B., Casey, K. S., Schlax, M. G.: Daily

576 High-Resolution-Blended Analyses for Sea Surface Temperature, *J. Climate*, 20, 5473-5496,

577 doi:10.1175/2007JCLI1824.1, 2007.

578 Sammon, J. W.: A non-linear mapping for data structure analysis, *IEEE Trans. Computers*, C-18,

579 401–409 , 1969.

580 Sato, K., Inoue, J., and Watanabe, M.: Influence of the Gulf Stream on the Barents Sea ice retreat and

581 Eurasian coldness during early winter, *Environ. Res. Lett.*, 9, 084009,

582 doi:10.1088/1748-9326/9/8/084009, 2014.

583 Schudeboom, A., McDonald, A. J., Morgenstern, O., Harvey, M., and Parsons, S.: Regional
584 regime-based evaluation of present-day GCM cloud simulations using self-organizing maps, *J.*
585 *Geophys. Res. Atmos.*, 123, 4259–4272, doi:10.1002/2017JD028196, 2018.

586 Screen, J. A. and Simmonds, I.: The central role of diminishing sea ice in recent Arctic temperature
587 amplification, *Nature*, 464, 1334-1337, doi:10.1038/nature09051, 2010.

588 Screen, J. S. and Simmonds, I.: Erroneous Arctic temperature trends in the ERA-40 reanalysis: A closer
589 look, *J. Clim.*, 24, 2620–2627, doi:10.1175/2010JCLI4054.1, 2011.

590 Sedlar, J., Tjernström, M., Mauritsen, T., Shupe, M. D., Brooks, I. M., Persson, O., Birch, C. E., Leck,
591 C., Sirevaag, A., and Nicolaus, M. : A transitioning Arctic surface energy budget: The impacts of
592 solar zenith angle, surface albedo and cloud radiative forcing, *Clim. Dyn.*, 37, 1643–1660,
593 doi:[10.1007/s00382-010-0937-5](https://doi.org/10.1007/s00382-010-0937-5), 2011.

594 Shepherd, T. G.: Effects of a warming Arctic, *Science*, 353, 989-990, doi:10.1126/science.aag2349,
595 2016.

596 Simmons, A., and Poli, P.: Arctic warming in ERA-Interim and other analyses, *Q. J. R. Meteorol. Soc.*,
597 141, 1147-1162, doi:10.1002/qj.2422, 2015.

598 Skific, N., Francis, J. A., and Cassano, J. J.: Attribution of projected changes in atmospheric moisture
599 transport in the Arctic: A self-organizing map perspective, *J. Clim.*, 22, 4135-4153,
600 doi:10.1175/2009JCLI2645.1, 2009.

601 Sorokina, S. A., Li, C., Wettstein, J. J., and Kvamstø, N. G.: Observed atmospheric coupling between
602 Barents sea ice and the warm-Arctic cold-Siberian anomaly pattern, *J. Clim.*, 29, 495-511,
603 doi:10.1175/JCLI-D-15-0046.1, 2016.

604 Stroeve, J. C., , Holland, M. M., Meier, W., Scambos, T., and Serreze, M.: Arctic sea ice decline: faster
605 than forecast, *Geophys. Res. Lett.*, 34, L09051, doi:10.1029/2007gl029703, 2007.

606 Stroeve, J. C.: Trends in Arctic sea ice extent from CMIP5, CMIP3 and observations, *Geophys. Res.*
607 *lett.*, 39, L16502, doi:10.1029/2012GL052676 , 2012.

608 Sun, L., Perlitz, J., and Hoerling, M.: What caused the recent “warm Arctic-Cold Continents” trend
609 pattern in winter temperature?, *Geophys. Res. Lett.*, 43, 5345-5352,
610 doi:10.1002/2016GL069024, 2016.

611 Sung, M.-K., Kim, S.-H., Kim, B.-M., and Choi, Y.-S.: Interdecadal variability of the warm Arctic and
612 cold Eurasia pattern and its North Atlantic origin, *J. Clim.*, 31, 5793-5810,
613 doi:10.1175/JCLI-D-17-0562.1, 2018.

614 Tang, Q., Zhang, X., Yang, X., and Francis J. A.: Cold winter extremes in northern conditions linked to
615 Arctic sea ice loss, *Environ. Res. Lett.*, 8, 014036, doi:1088/1748-9326/8/1/014036 ,2013.

616 Takaya K., and Nakamura, H.: A formulation of a phase-independent wave-activity flux for stationary
617 and migratory quasigeostrophic eddies on a zonally varying basic flow, *J. Atmos. Sci.*, 58,
618 608-627, 2001.

619 Uppala, S., KÅllberg, P. W., Simmons, A. J., Andrae, U., Da Costa Bechtold, V., Florino, M., Gibson, J.
620 K., Haseler, J., Hernandez, A., Kelly, G. A., Li, X., Onogi, K., Saarinen, S., Sokka, N., Allan, R.
621 P., Andersson, E., Arpe, K., Balmaseda, M. A., Beljaars, A. C. M., Van De Berg, L., Bidlot, J.,
622 Bormann, N., Caires, S., Chevallier, F., Dethof, A., Dragosavac, M., Fisher, M., Fuentes, M.,
623 Hagemann, S., H ölm, E., Hoskins, B. J., Isaksen, L., Janssen, P. A. E. M., Jenne, R., Mcnally, A.
624 P., Mahfouf, J.-F., Morcrette, J.-J., Rayner, N. A., Saunders, R. W., Simon, P., Sterl, A.,
625 Trenberth, K. E., Untch, A., Vasiljevic, D., Viterbo, P., and Woollen, J.: The ERA-40 re-analysis,

626 Quarterly Journal of the Royal Meteorological Society, 131, 2961–3012, doi:10.1256/qj.04.176.

627 2005.

628 Walsh, J. E.: Intensified warming of the Arctic: Causes and impacts on middle Latitudes, *Glob. Planet.*

629 *Change*, 117, 52–63, doi:10.1016/j.gloplacha.2014.03.003 , 2014.

630 Vihma, T.: Effects of Arctic sea ice decline on weather and climate: A review, *Surv. Geophys.*, 35,

631 1175–1214, doi:10.1007/s10712-014-9284-0 , 2014.

632 Vihma, T., Graversen, R., Chen, L., Handorf, D., Skific, N., Francis, J. A., Tyrrell, N., Hall, R., Hanna,

633 E., Uotila, P., Dethloff, K., Karpechko, A. Y., Björnsson, H., and Overland, J. E.: Effects of the

634 tropospheric large-scale circulation on European winter temperatures during the period of amplified

635 Arctic warming, *Int. J. Climatol.*, doi:10.1002/joc.6225, 2019.

636 Wang, C., Graham, R. M., Wang, K., Gerland, S., Granskog, M. A.: Comparison of ERA5 and

637 ERA-Interim near-surface air temperature, snowfall and precipitation over Arctic sea ice: effects

638 on sea ice thermodynamics and evolution, *The Cryosphere*, 13, 1661–1679, 2019.

639 Yoo, C., Feldstein, S., and Lee, S.: The impact of the Madden–Julian oscillation trend on the Arctic

640 amplification of surface air temperature during the 1979–2008 boreal winter, *Geophys. Res.*

641 *Lett.*, 38, L24804, doi:10.1029/2011GL049881, 2011.

642 Yu, L., Zhong, S., Winkler, J. A., Zhou, M., Lenschow, D. H., Li, B., Wang, X., and Yang, Q.: Possible

643 connections of the opposite trends in Arctic and Antarctic sea-ice cover, *Scientific Reports*, 7,

644 45804, doi:10.1038/srep45804, 2017.

645

646

647

648 Table 1. Spatial correlations (Corrs) between the daily winter (DJF) surface air
649 temperature and the corresponding SOM pattern for each day from 1979 to 2018.

	3×1	2×2	3×2	4×2	3×3	5×2	4×3	5×3	4×4
Corr	0.26	0.43	0.48	0.48	0.50	0.49	0.50	0.51	0.51

650

651

652

653

654

655

656

657

658

659

660

661

662

663

664

665

666

667

668

669

670

671

672

673

674

675

676

677

678

679

680 Table 2. Averaged anomalous NAO and AO indices for all occurrences of each SOM
681 node. Asterisks indicate the above 95% confidence level.

682

	Node1	Node2	Node3	Node4	Node5	Node6	Node7	Node8	Node9
NAO	0.38*	0.22*	0.12*	0.05	-0.22*	-0.02	-0.07	-0.31*	-0.32*
AO	0.44*	0.38*	1.03*	-0.42	-0.62*	0.22*	-0.44*	-1.11*	-0.41*

683

684

685

686

687

688

689

690

691

692

693

694

695

696

697

698

699

700

701

702

703

704

705

706

707

708

709

710

711

712

713

714

715

716

717

718

719

720

721 Table 3. Trends in the frequency of occurrences for each SOM node (day yr⁻¹).
722 Asterisks indicate the above 95% confidence level.

723

	Node1	Node2	Node3	Node4	Node5	Node6	Node7	Node8	Node9
Trend	0.80*	0.10	-0.18	0.22*	-0.02	-0.39*	0.17	-0.17	-0.50*

724

725

726

727

728

729

730

731

732

733

734

735

736

737

738

739

740

741

742

743

744

745

746

747

748

749

750

751

752

753

754

755

756

757

758

759

760

761 Table 4. Frequencies of occurrence (%) of wintertime surface air temperature patterns
762 in Figure 1 for all winters before 1998 and after 1998 for the period 1979-2019.
763 Values with Asterisks are significantly different from climatology above the 95%
764 confidence level.

SOM patterns	Frequencies of occurrence		
	All winters	Winters before 1998	Winters after 1998
Node 1	17.1	7.4*	26.8
Node 2	4.4	3.3	5.4
Node 3	17.2	18.8	15.6
Node 4	8.6	5.4	11.7
Node 5	3.4	3.4	3.5
Node 6	10.2	15.2*	2.1*
Node 7	13.7	10.6	16.8
Node 8	10.1	12.1	8.0
Node 9	15.4	23.7*	7.1*

766
767
768
769
770
771
772
773
774
775
776
777
778
779
780
781
782
783
784
785
786
787
788
789
790
791
792

793 **Figure Captions**

794 Figure 1. Spatial patterns of SOM nodes for daily wintertime (December, January, and
795 February) surface air temperature anomalies (°C) ~~without removing their linear trends~~
796 from ERA-Interim reanalysis over the 1979-2019 period. The number in brackets
797 denotes the frequency of the occurrence for each node.

798 Figure 2. Corresponding 500-hPa geopotential height anomalies (gpm) ~~without~~
799 ~~removing their linear trends~~ from ERA-Interim reanalysis over the 1979-2019 period
800 for each node in Figure 1. Dotted regions indicate the above 95% confidence level.
801 The ~~sub-domain in 1thick black lines~~ shows the study region.

802 Figure 3. Corresponding anomalous 850-hPa wind field (ms^{-1}) ~~without removing its~~
803 ~~linear trend~~ from ERA-Interim reanalysis over the 1979-2019 period for each node in
804 Figure 1. Shaded regions indicate the above 95% confidence level. ~~The thick black~~
805 ~~lines show the study region.~~

806 Figure 4. Corresponding anomalous daily accumulated downward longwave radiation
807 (105 $W m^{-2}$) ~~without removing its linear trend~~ from ERA-Interim reanalysis over the
808 1979-2019 period for each node in Figure 1. Dotted regions indicate the above 95%
809 confidence level. ~~The thick black lines denote show the study region.~~

810 Figure 5. Corresponding anomalous daily accumulated turbulent heat flux (sensible
811 and latent heat) ($10^5 W m^{-2}$) ~~without removing their linear trends~~ from ERA-Interim
812 reanalysis over the 1979-2019 period for each node in Figure 1. Positive values
813 denote heat flux from atmosphere to ocean and vice versa. Dotted regions indicate the
814 above 95% confidence level. ~~The thick black lines denote show the study region.~~

815 Figure 6. Corresponding anomalous wintertime sea ice concentration ~~without~~
816 ~~removing its linear trend~~ from the NSIDC over the 1979-2019 period for each node in

817 Figure 1. Dotted regions indicate the above 95% confidence level.

818 Figure 7. Time series of the number of days for occurrence of each SOM node in
819 Figure 1 over the 1979-2019 period. The ~~thick-red~~ lines denote the trend in time
820 series.

821 Figure 8. Total (top), SOM-explained (middle), and residual (bottom) trend in
822 wintertime (DJF) surface air temperature ($^{\circ}\text{C yr}^{-1}$) over the 1979-2019 period. Dots in
823 the top panel indicate above 95% confidence level.

824 Figure 9. Trends in surface air temperature explained by each SOM node ($^{\circ}\text{C yr}^{-1}$)
825 over the 1979-2019 period. The percentage in the upper of each panel indicates the
826 fraction of the total trend represented by each node.

827 Figure 10. Anomalous SST ($^{\circ}\text{C}$) ~~from the NOAA over the 1979-2019 period~~ regressed
828 into the normalized time series of occurrence number for nodes 1, 4, 6, and 9 ~~without~~
829 ~~removing its linear trend from the NOAA over the 1979-2019 period~~.

830 Figure 11. Anomalous 500-hPa geopotential height (gpm) ~~from ERA-Interim~~
831 ~~reanalysis over the 1979-2019 period~~ regressed into the normalized time series of
832 occurrence number for nodes 1, 4, 6, and 9 ~~without removing its linear trend from~~
833 ~~ERA-Interim reanalysis over the 1979-2019 period~~.

834 Figure 12. The anomalous wave activity flux (vectors) (Takaya and Nakamura, 2001)
835 and stream function (colors, units: $10^7 \text{ m}^2 \text{s}^{-1}$) ~~from ERA-Interim reanalysis over the~~
836 ~~1979-2019 period~~ regressed onto the normalized time series of occurrence number for

837 nodes 1, 4, 6, and 9 ~~without removing their linear trends from ERA-Interim reanalysis~~
838 ~~over the 1979-2019 period.~~

839 Figure 13. Spatial patterns of SOM nodes for detrended daily wintertime (December,
840 January, and February) surface air temperature anomalies (°C) from the 20CR
841 reanalysis for the 1851-2014 period. The number in brackets denotes the frequency of
842 the occurrence for each node.

843 Figure 14. Time series of the number of days for occurrence of each SOM node in
844 Figure 13 from the 20CR reanalysis for the 1851-2014 period. The thick red lines
845 denote the result in Figure 7 from the ERA-Interim reanalysis for the 1979-2019
846 period.

847 Figure 15. The (a) leading pattern and (b) its time series (PC1 and PC2) of EOF
848 analysis of wintertime surface air temperature anomalies from the 20CR reanalysis for
849 the 1851-2014 period. Prior to EOF analysis, surface air temperature data are
850 detrended. A 40-yr low-pass filter is applied to the time series of PC1, PC2, AMO,
851 PDO, and central North Pacific Ocean (CNPO) indices. The correlation coefficients
852 between PC1 and AMO, PDO and CNPO indices are -0.46 (p<0.0001), 0.38
853 (p<0.0001), and -0.19 (p=0.019); those between PC2 and AMO, PDO and CNPO
854 indices are -0.44 (p<0.0001), 0.38 (p<0.0001), and -0.26 (p=0.0009).

855

856

857

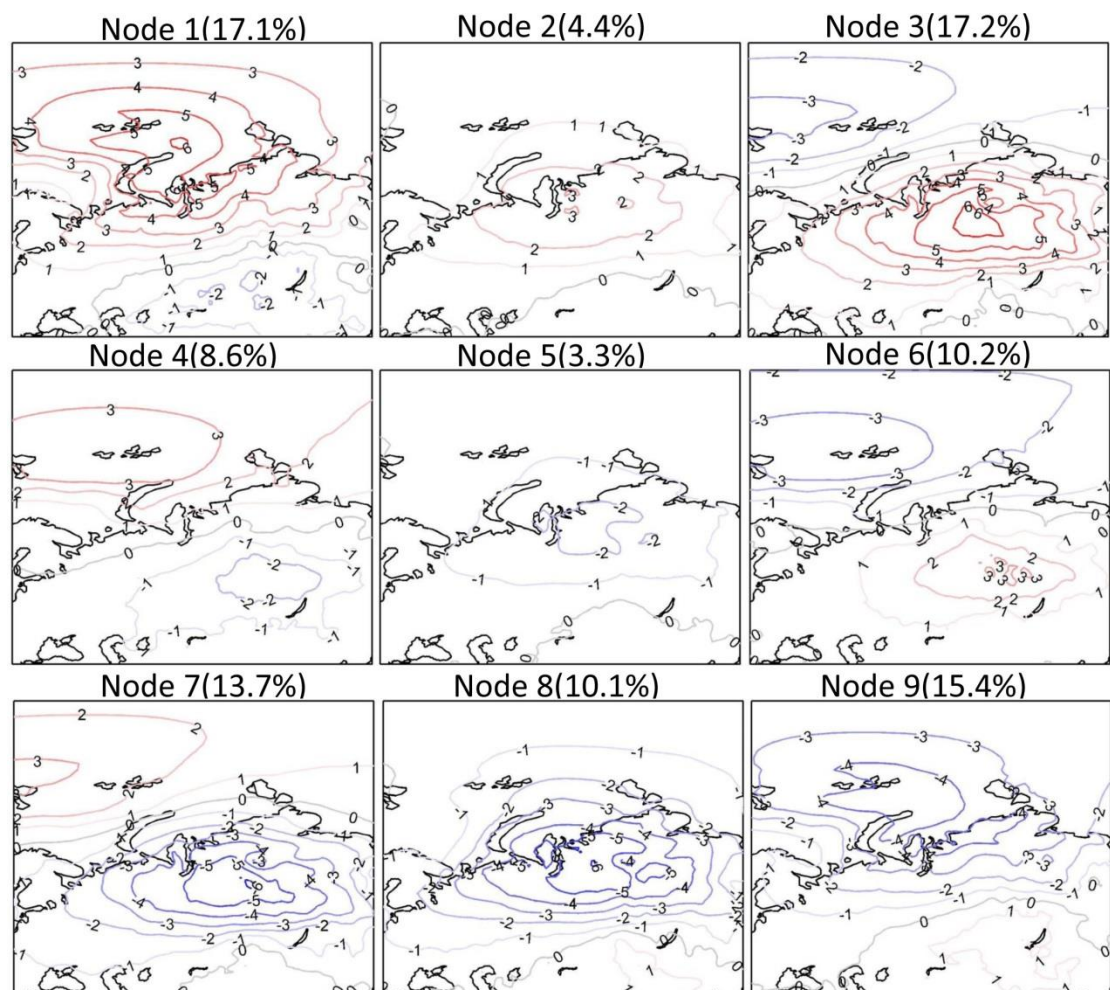
858

859

860

861

862



863

864 Figure 1. Spatial patterns of SOM nodes for daily wintertime (December, January, and February)
 865 surface air temperature anomalies ($^{\circ}\text{C}$) ~~without removing their linear trends~~ from ERA-Interim
 866 reanalysis over the 1979-2019 period. The number in brackets denotes the frequency of the
 867 occurrence for each node.

868

869

870

871

872

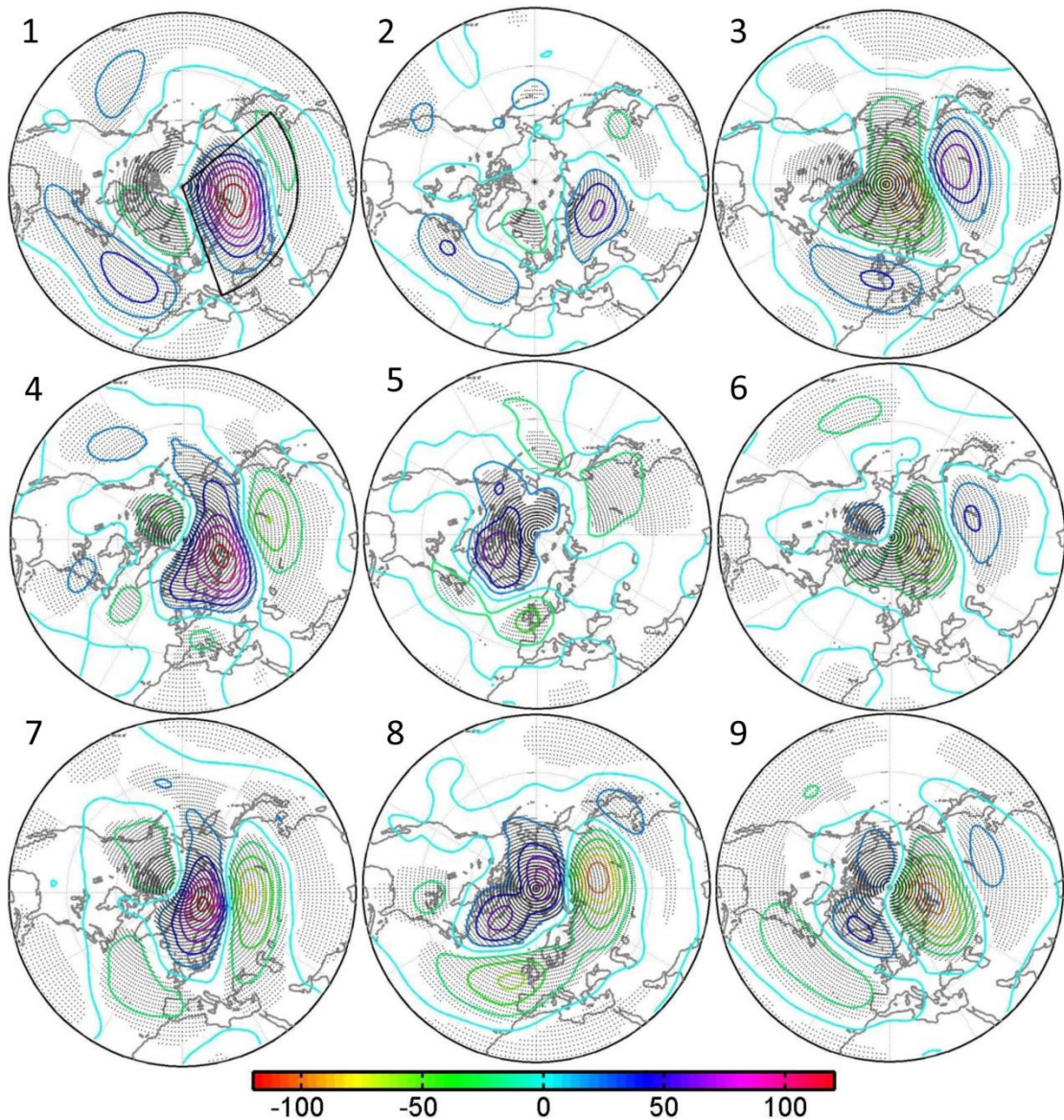
873

874

875

876

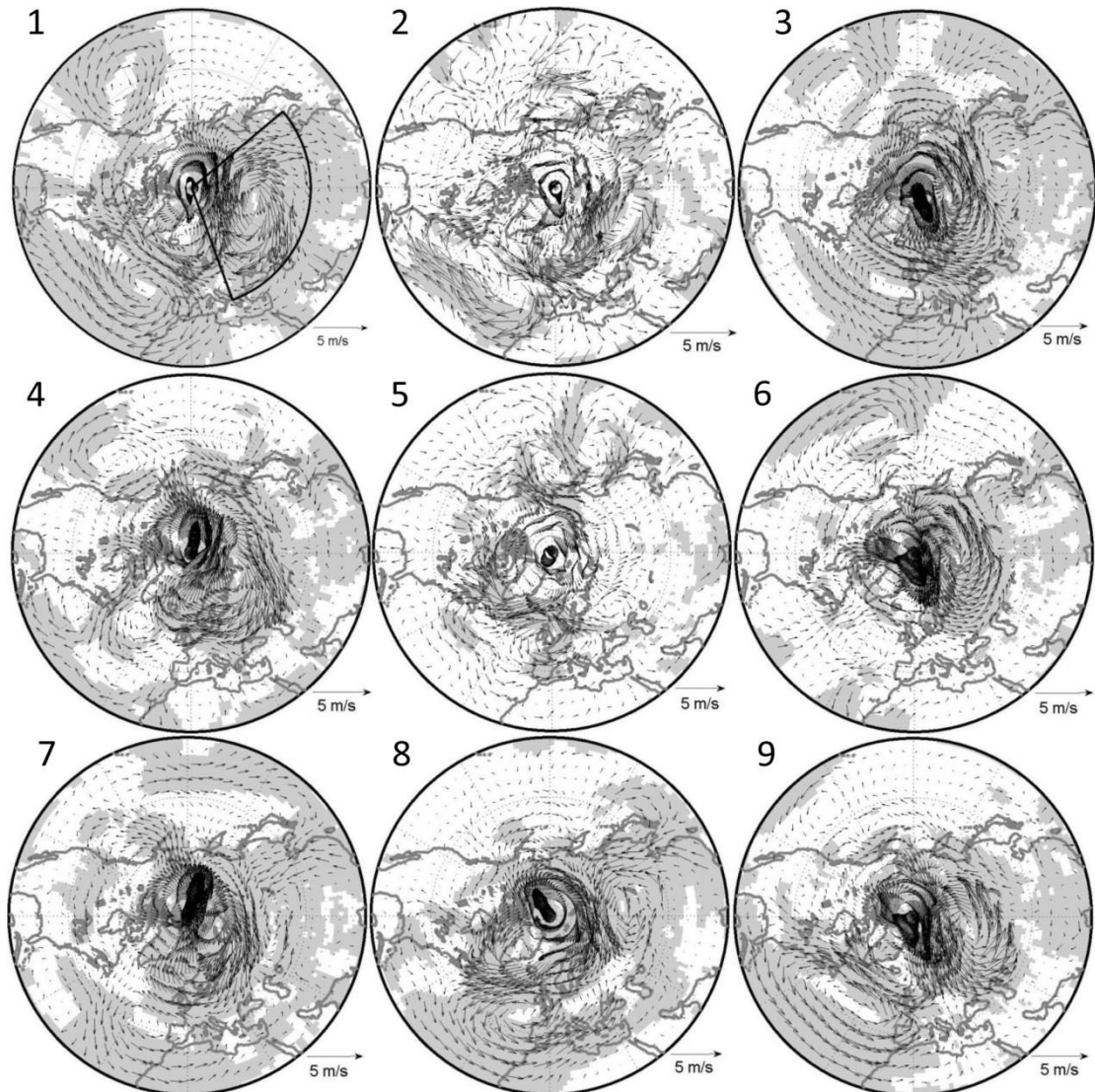
877
878
879
880
881
882
883



884
885 Figure 2. Corresponding 500-hPa geopotential height anomalies (gpm) ~~without removing their~~
886 ~~linear trends~~ from ERA-Interim reanalysis over the 1979-2019 period for each node in Figure 1.
887 Dotted regions indicate the above 95% confidence level. The sub-domain in 1thick black lines
888 ~~shows~~ the study region.

889
890
891
892
893

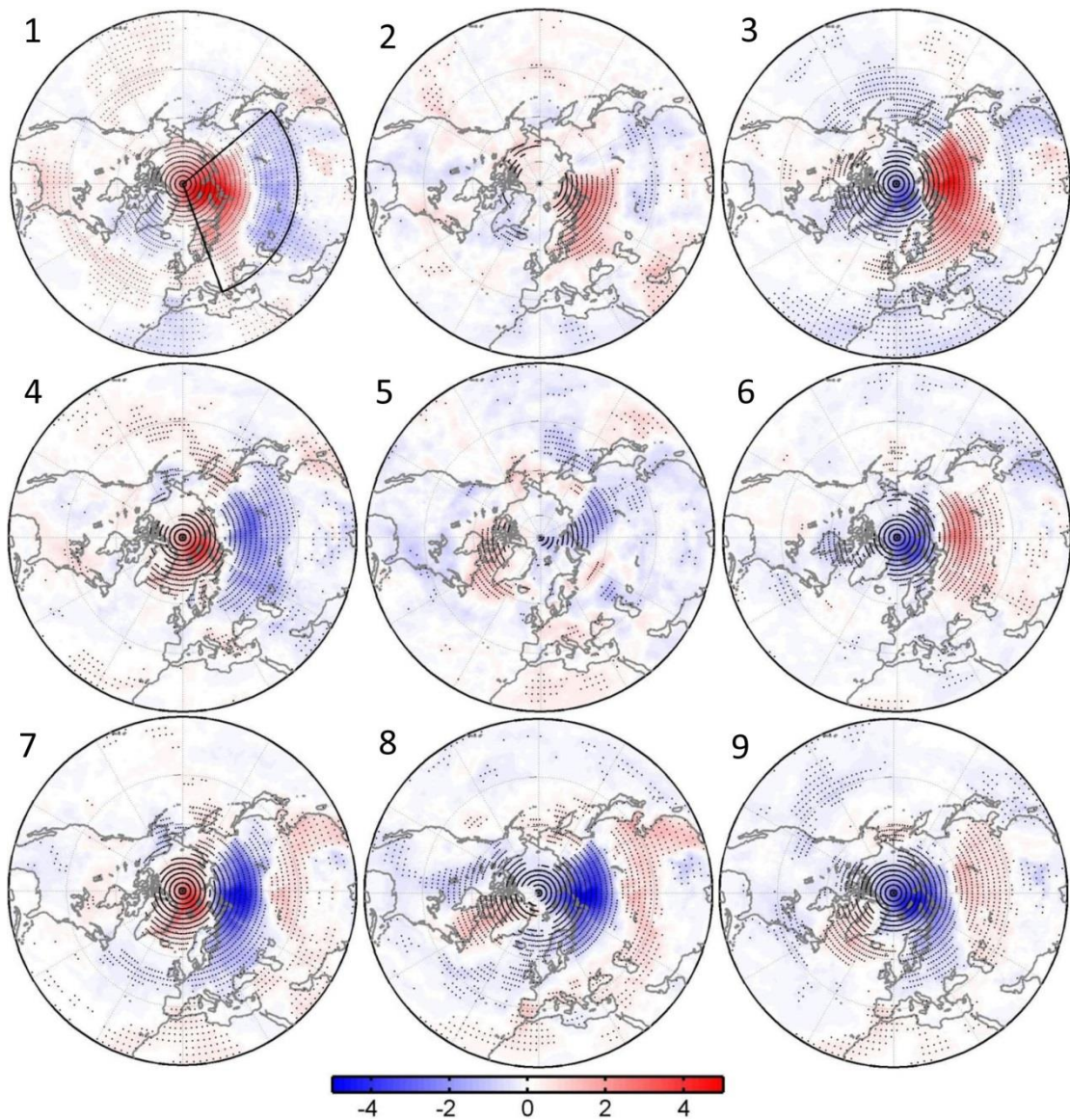
894
895
896
897
898



899
900
901
902
903
904
905
906
907
908
909
910
911

Figure 3. Corresponding anomalous 850-hPa wind field ~~without removing its linear trend~~ from ERA-Interim reanalysis over the 1979-2019 period for each node in Figure 1. Shaded regions indicate the above 95% confidence level. ~~The thick black lines show the study region.~~

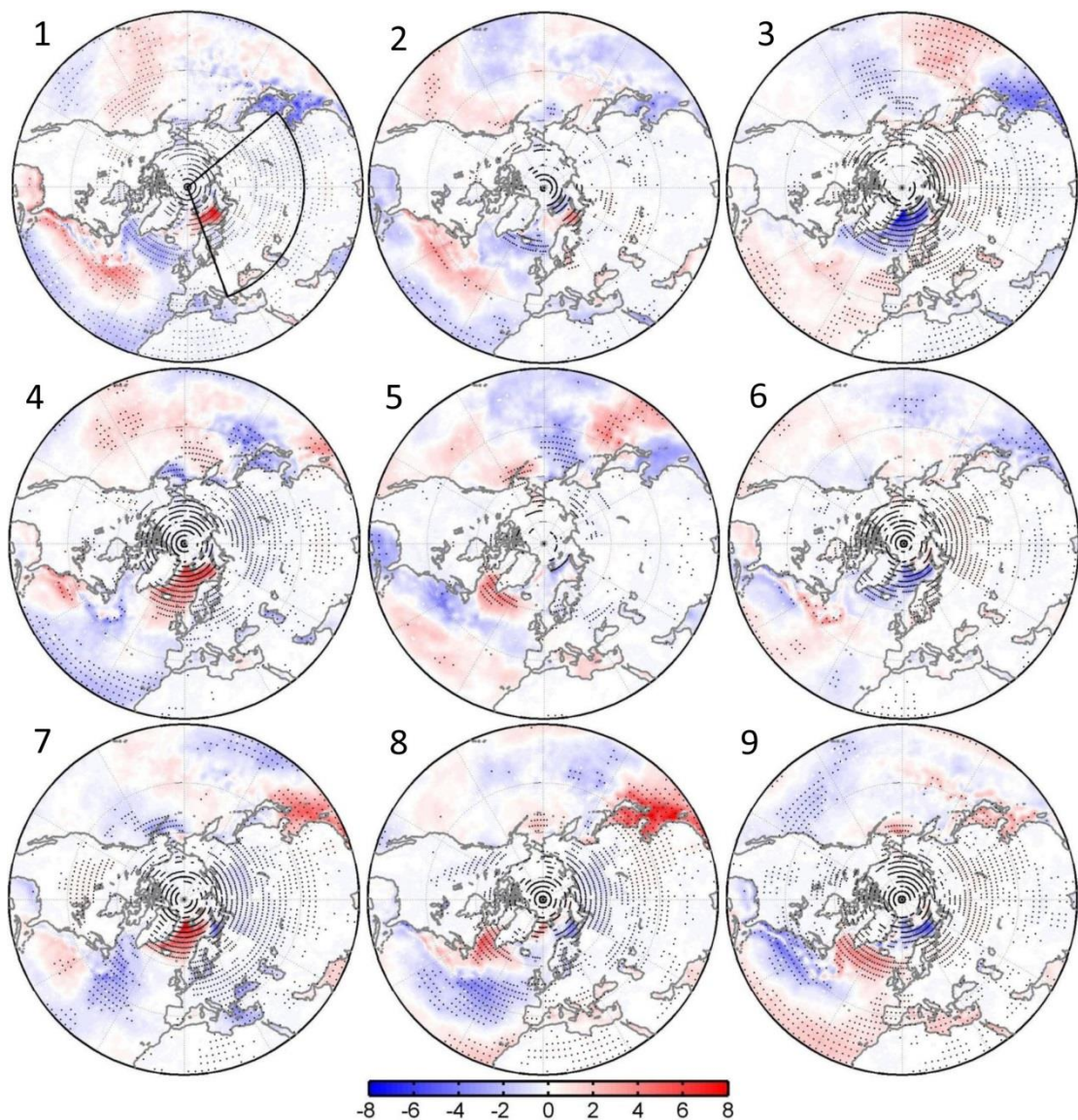
912
913
914
915
916
917
918



919
920 Figure 4. Corresponding anomalous daily accumulated downward longwave radiation (10^5 W m^{-2})
921 ~~without removing its linear trend~~ from ERA-Interim reanalysis over the 1979-2019 period for each
922 node in Figure 1. Dotted regions indicate the above 95% confidence level. ~~The thick black lines~~
923 ~~show the study region.~~

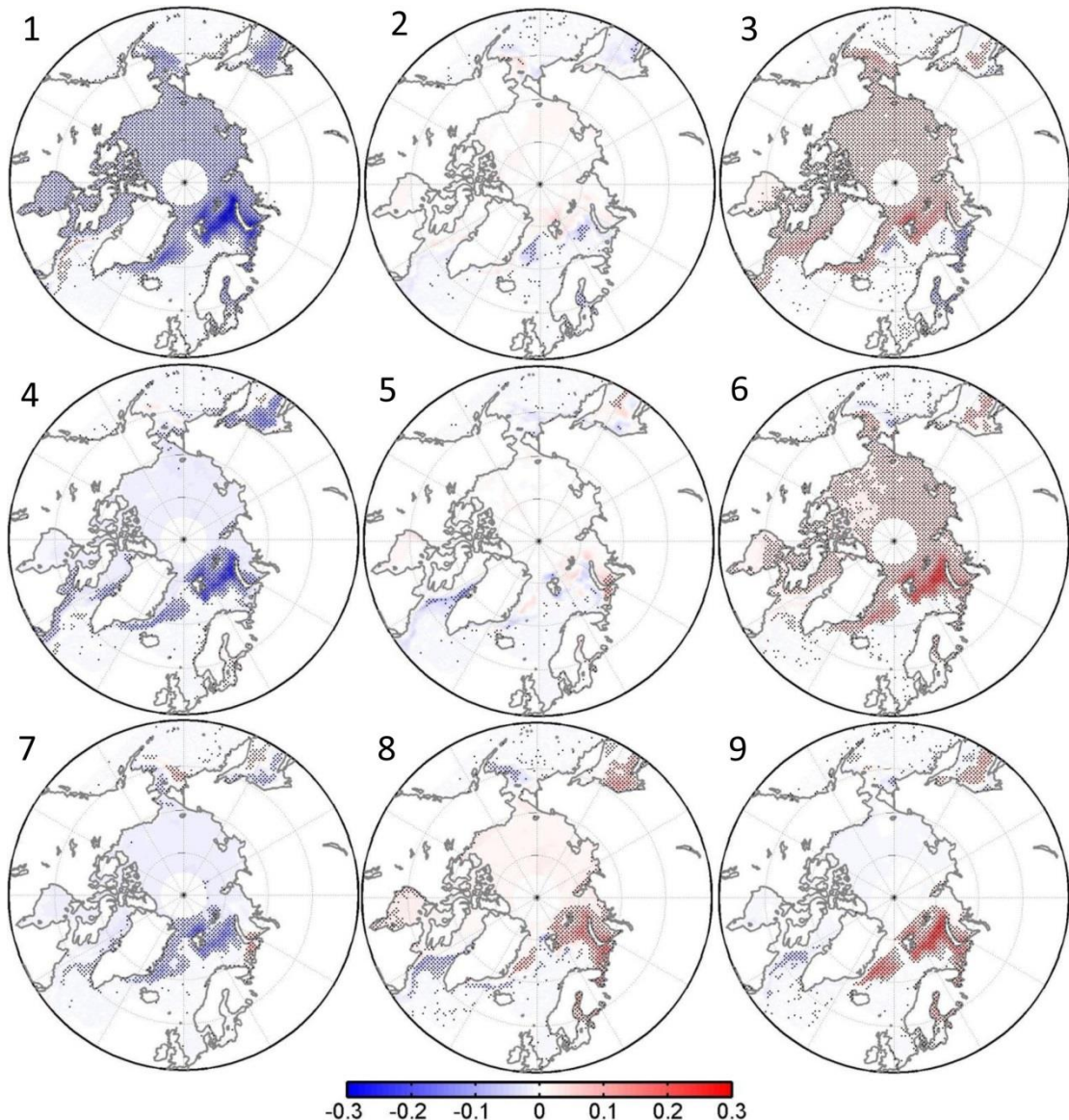
924
925
926
927
928

929
930
931
932
933
934
935
936
937
938



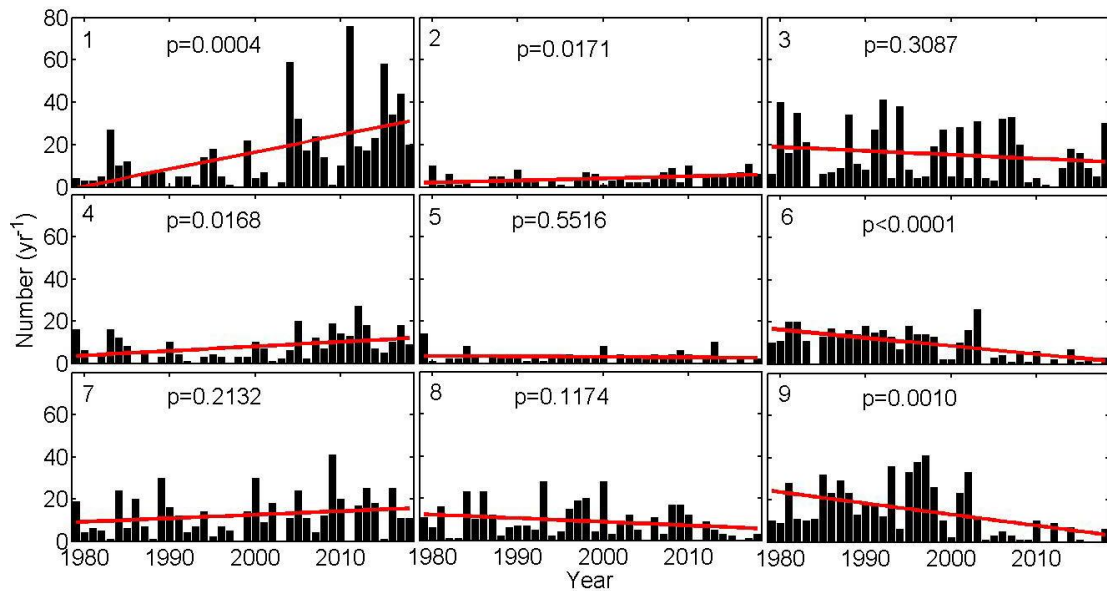
939
940 Figure 5. Corresponding anomalous daily accumulated turbulent heat flux (sensible and latent heat)
941 (10^5 W m^{-2}) ~~without removing their linear trends~~ from ERA-Interim reanalysis over the 1979-2019
942 period for each node in Figure 1. Positive values denote heat flux from atmosphere to ocean and
943 vice versa. Dotted regions indicate the above 95% confidence level. ~~The thick black lines show~~
944 ~~the study region.~~
945

946
947
948
949
950
951



952
953 | Figure 6. Corresponding anomalous wintertime sea ice concentration **without removing its linear**
954 | **trend**—from the NSIDC over the 1979–2019 period for each node in Figure 1. Dotted regions
955 | indicate the above 95% confidence level.
956
957
958
959
960
961
962

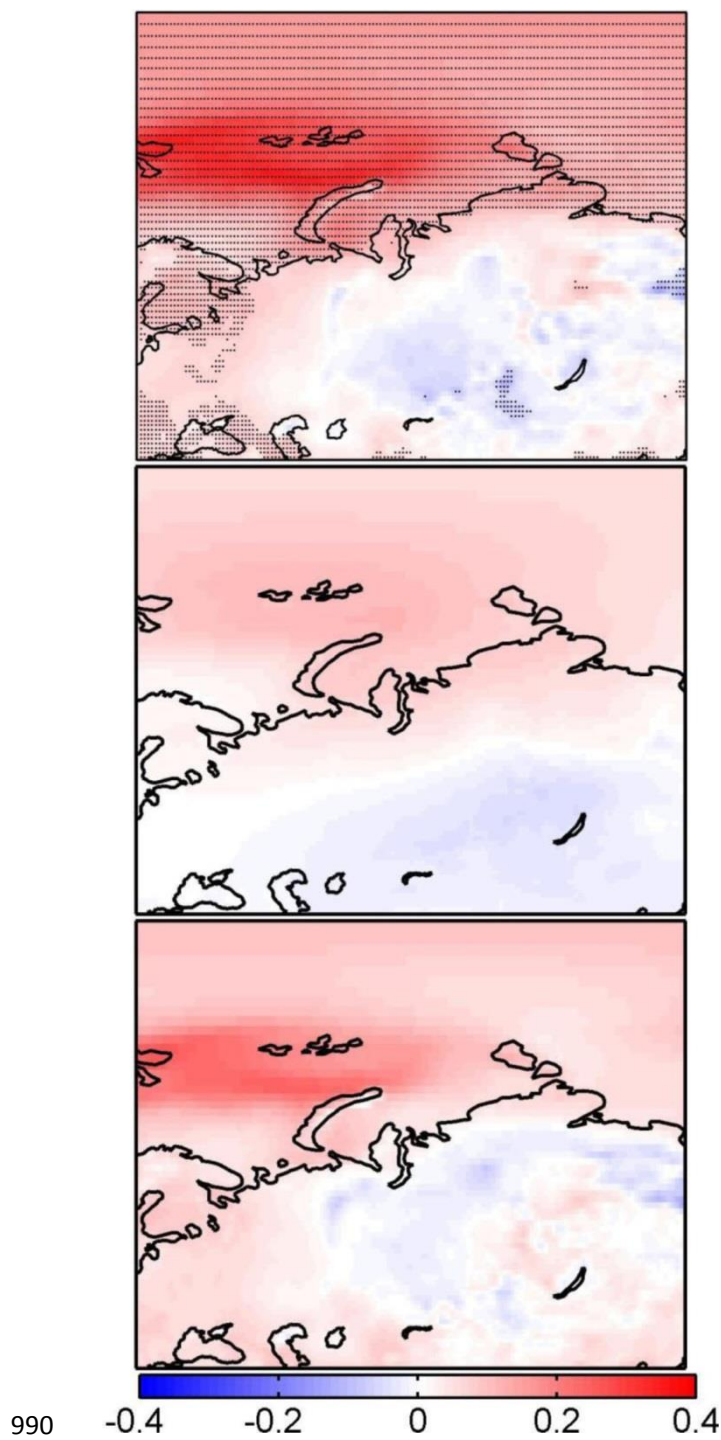
963
964
965
966
967
968
969
970
971



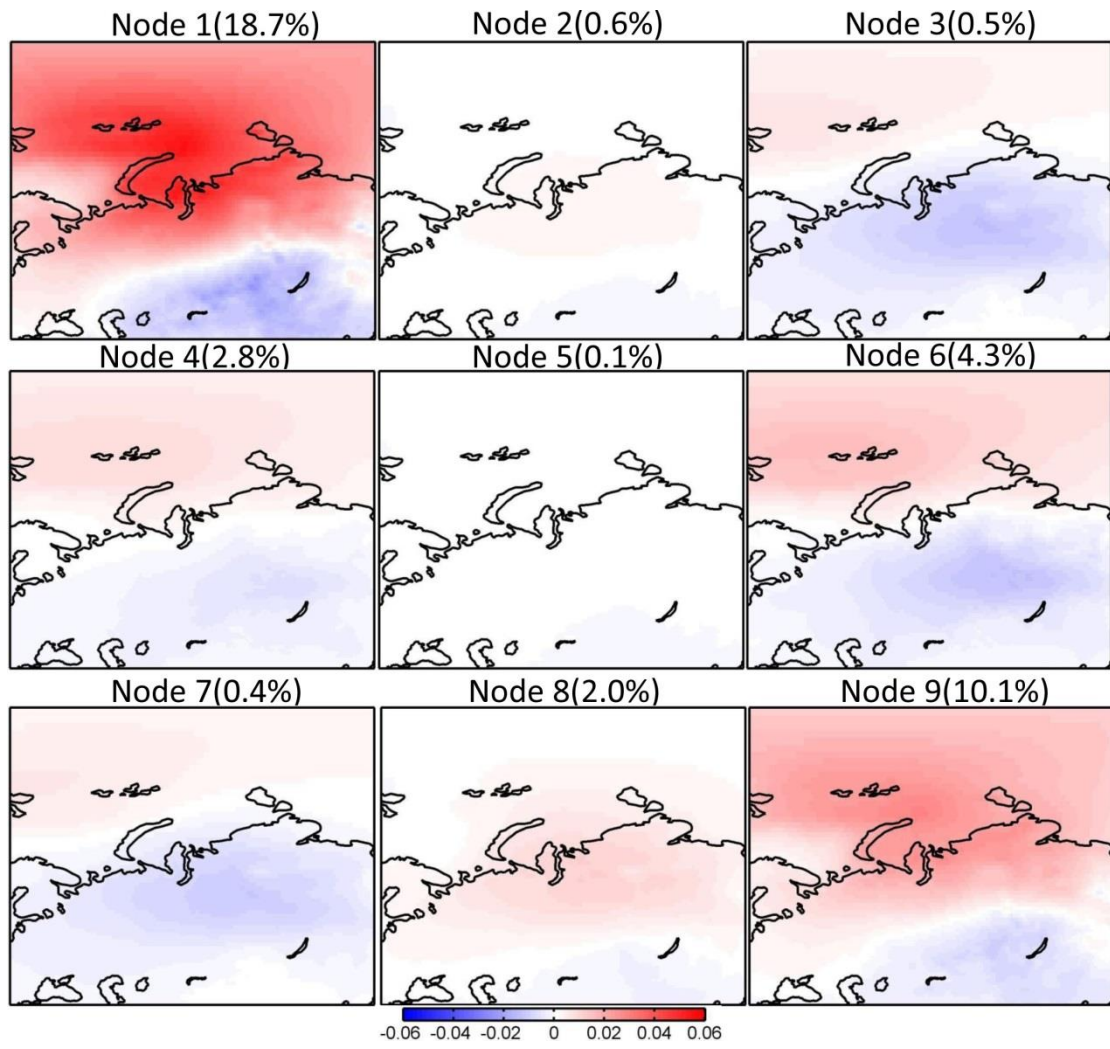
972

973 | Figure 7. Time series of the number of days for occurrence of each SOM node in Figure 1 over the
974 | 1979-2019 period. The thick-red lines denote the trend in time series.

975
976
977
978
979
980
981
982
983
984
985
986
987
988
989



990
991 Figure 8. Total (top), SOM-explained (middle), and residual (bottom) trend in wintertime (DJF)
992 surface air temperature ($^{\circ}\text{C yr}^{-1}$) over the 1979-2019 period. Dots in the top panel indicate above
993 95% confidence level.
994



995
996 Figure 9. Trends in surface air temperature explained by each SOM node ($^{\circ}\text{C yr}^{-1}$) over the
997 1979-2019 period. The percentage in the upper of each panel indicates the fraction of the total
998 trend represented by each node.

999

1000

1001

1002

1003

1004

1005

1006

1007

1008

1009

1010

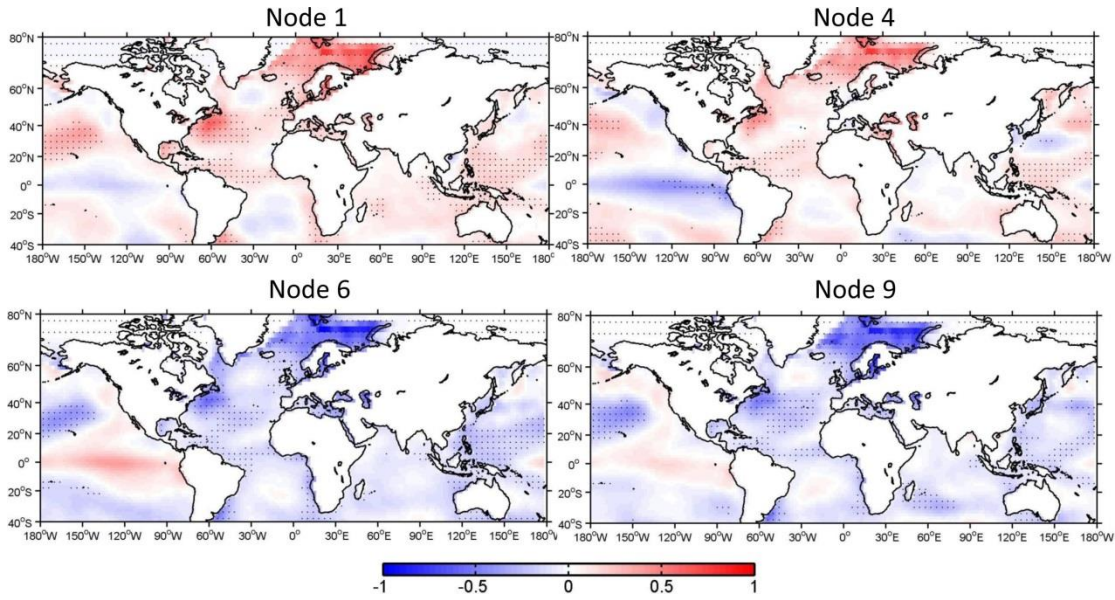
1011

1012

1013

1014

1015
1016



1017

1018 Figure 10. Anomalous SST ($^{\circ}$ C) [from the NOAA over the 1979-2019 period](#) regressed into the
1019 normalized time series of occurrence number for nodes 1, 4, 6, and 9 [without removing its linear](#)
1020 [trend from the NOAA over the 1979-2019 period](#).

1021

1022

1023

1024

1025

1026

1027

1028

1029

1030

1031

1032

1033

1034

1035

1036

1037

1038

1039

1040

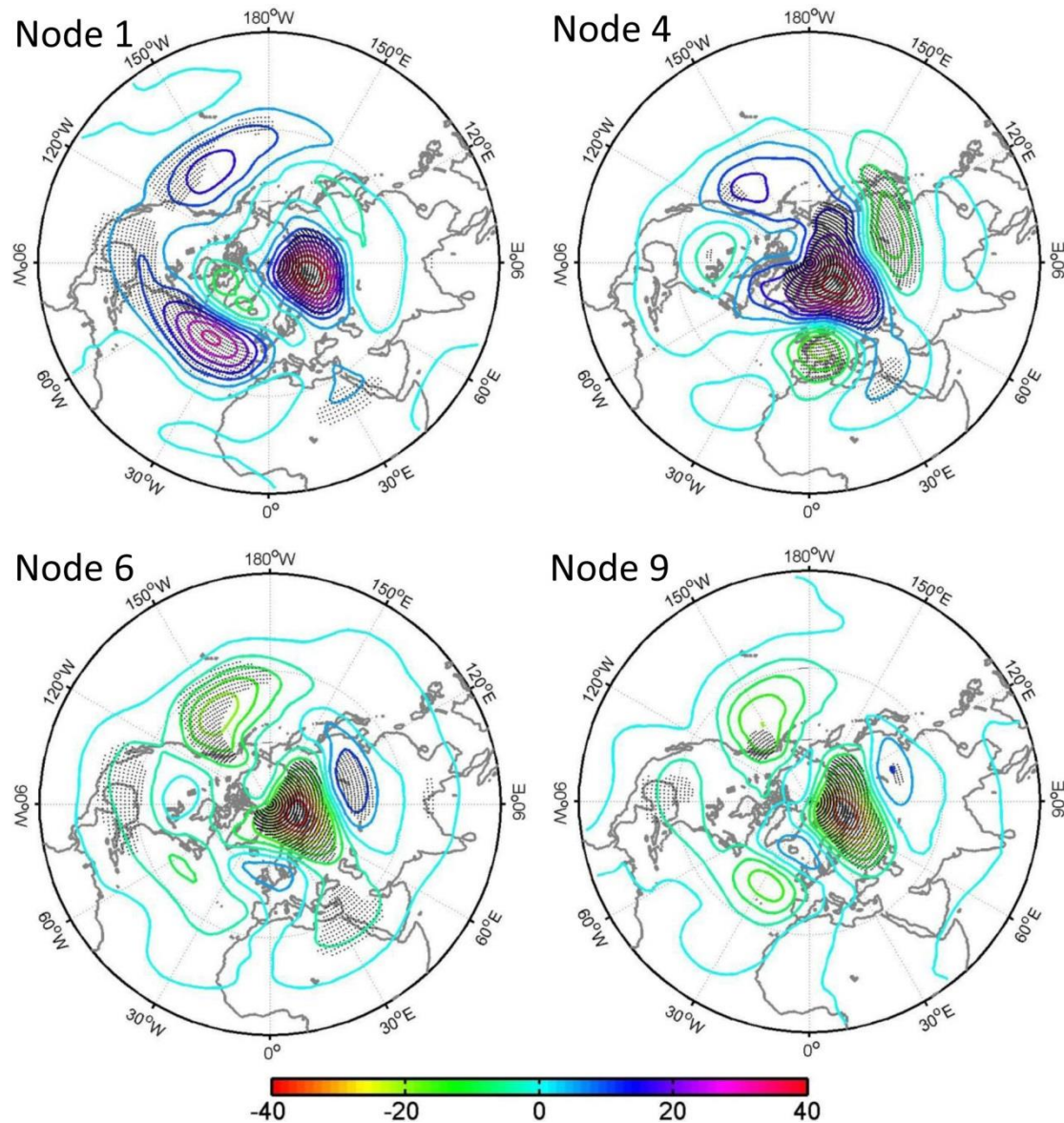
1041

1042

1043

1044

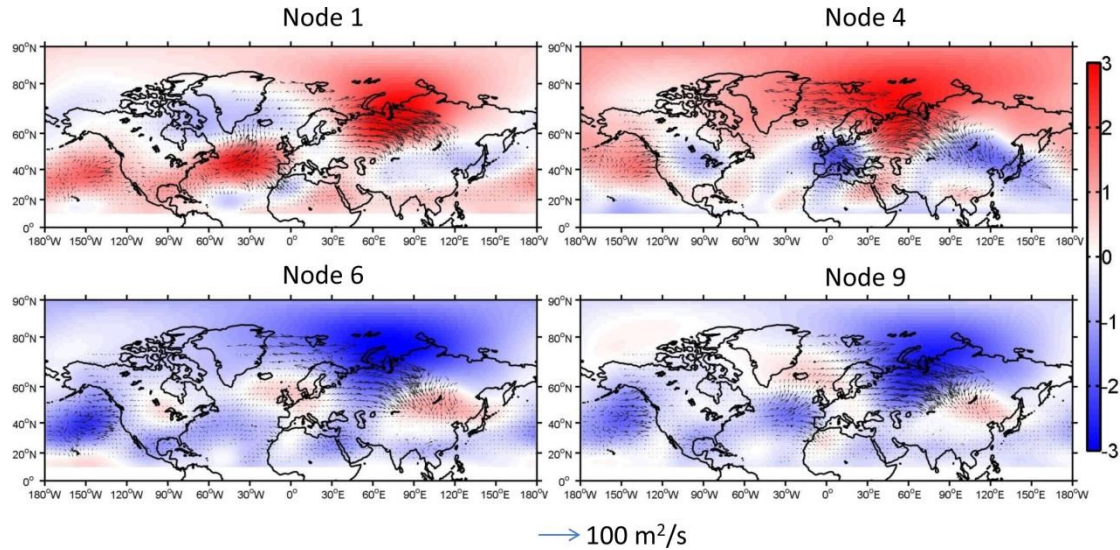
1045
1046
1047
1048



1050 Figure 11. Anomalous 500-hPa geopotential height (gpm) [from ERA-Interim reanalysis over the](#)
1051 [1979-2019 period regressed into the normalized time series of occurrence number for nodes 1, 4, 6,](#)
1052 [and 9 without removing its linear trend from ERA-Interim reanalysis over the 1979-2019 period.](#)

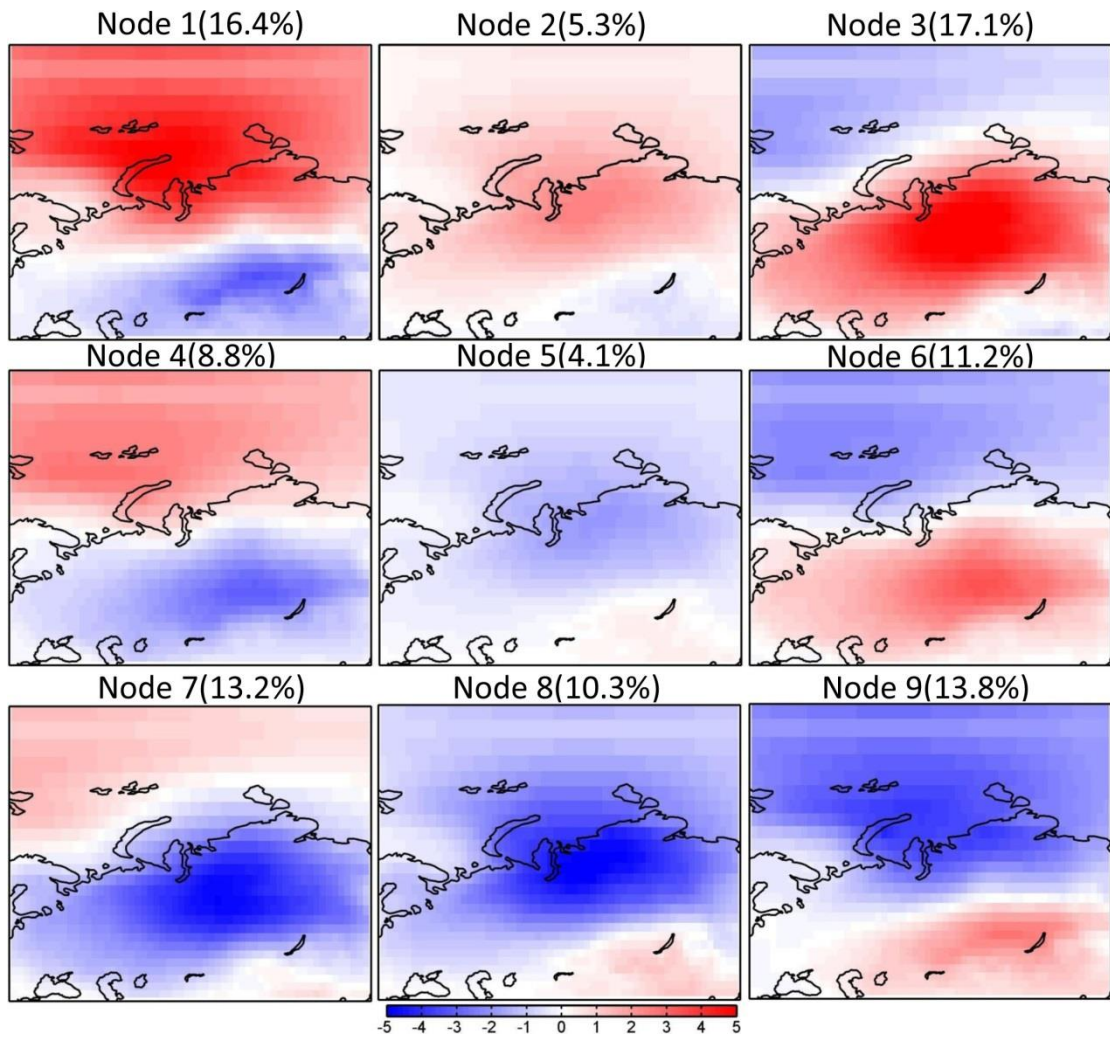
1053
1054
1055
1056
1057
1058
1059
1060

1061
1062
1063
1064
1065



1066
1067
1068
1069
1070
1071
1072
1073
1074
1075
1076
1077
1078
1079

Figure 12. The anomalous wave activity flux (vectors) (Takaya and Nakamura, 2001) and stream function (colors, units: $10^7 \text{ m}^2 \text{s}^{-1}$) [from ERA-Interim reanalysis over the 1979-2019 period](#) regressed onto the normalized time series of occurrence number for nodes 1, 4, 6, and 9 [without removing their linear trends from ERA-Interim reanalysis over the 1979-2019 period](#).



1080
1081 Figure 13. Spatial patterns of SOM nodes for detrended daily wintertime (December, January, and
1082 February) surface air temperature anomalies (°C) from the 20CR reanalysis for the 1851-2014
1083 period. The number in brackets denotes the frequency of the occurrence for each node.
1084
1085
1086
1087
1088
1089
1090
1091
1092
1093
1094
1095
1096
1097
1098
1099
1100

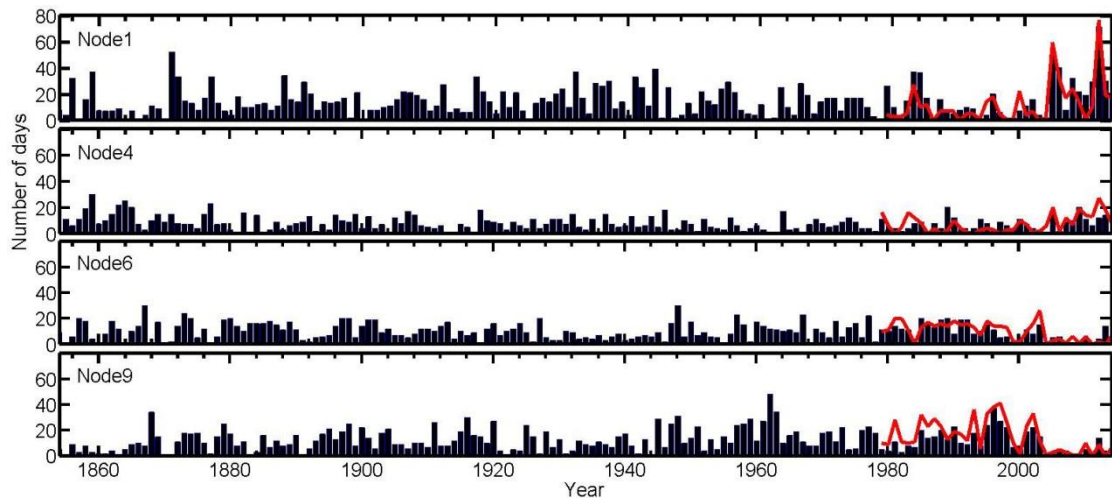


Figure 14. Time series of the number of days for occurrence of each SOM node in Figure 13 from the 20CR reanalysis for the 1851-2014 period. The thick red lines denote the result in Figure 7 from the ERA-Interim reanalysis for the 1979-2019 period.

1101

1102

1103

1104

1105

1106

1107

1108

1109

1110

1111

1112

1113

1114

1115

1116

1117

1118

1119

1120

1121

1122

1123

1124

1125

1126

1127

1128

1129

1130

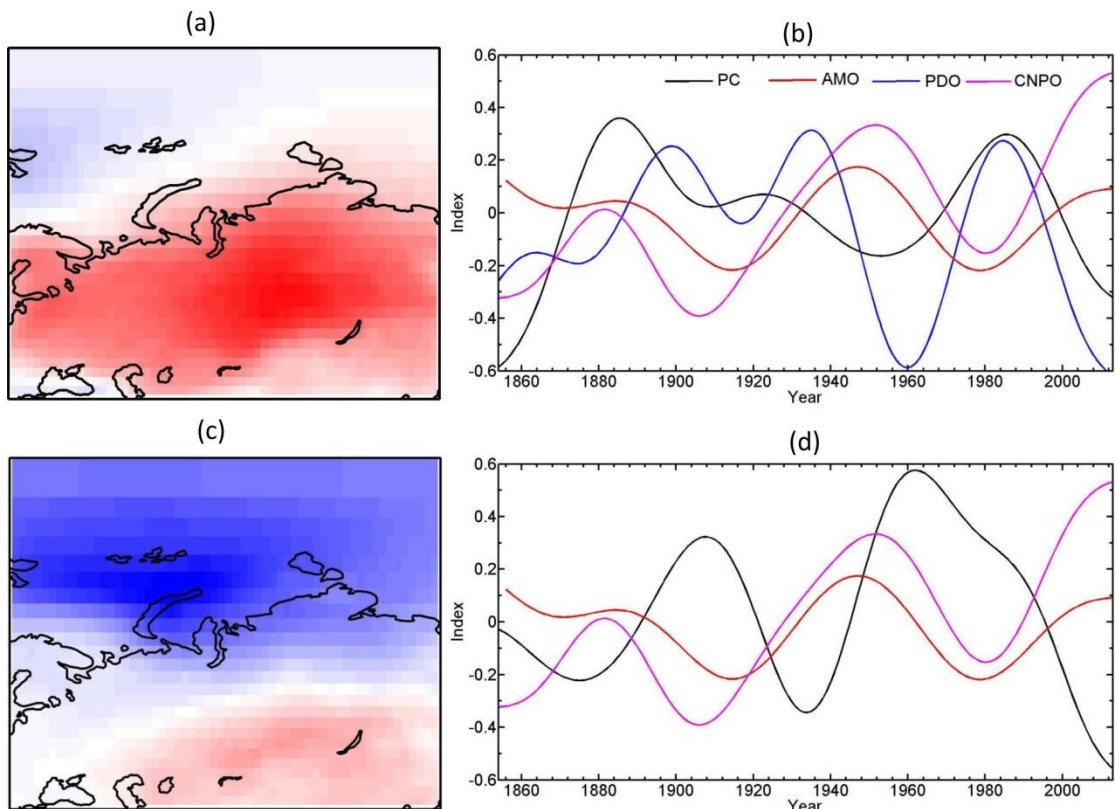
1131

1132

1133

1134

1135



1136

Figure 15. The (a) leading pattern and (b) its time series (PC1 and PC2) of EOF analysis of wintertime surface air temperature anomalies from the 20CR reanalysis for the 1851-2014 period.. Prior to EOF analysis, surface air temperature data are detrended. A 40-yr low-pass filter is applied to the time series of PC1, PC2, AMO, PDO, and central North Pacific Ocean (CNPO) indices. The correlation coefficients between PC1 and AMO, PDO and CNPO indices are -0.46 ($p<0.0001$), 0.38 ($p<0.0001$), and -0.19 ($p=0.019$); those between PC2 and AMO, PDO and CNPO indices are -0.44 ($p<0.0001$), 0.38 ($p<0.0001$), and -0.26 ($p=0.0009$).

1144